Mon. Not. R. Astron. Soc. **270,** 271–297 (1994)

Velocity profiles of galaxies with claimed black holes – III. Observations and models for M87

Roeland P. van der Marel★
Sterrewacht Leiden, Postbus 9513, 2300 RA Leiden, The Netherlands

Accepted 1994 April 18. Received 1994 April 7

ABSTRACT

We report on high-S/N subarcsec resolution spectra of M87, obtained with the 4.2-m William Herschel Telescope in the spectral regions around the blue G-band and the IR Ca II triplet. From the spectra we determine the line strengths, the mean and dispersion of the best-fitting Gaussian velocity profiles (i.e. the line-of-sight velocity distributions) and the Gauss–Hermite moments $h_3,\ldots h_6$ that measure deviations from a Gaussian. We find that the main results derived from the two spectral regions agree, in contradiction to recent measurements by Jarvis & Melnick. The observed line strengths have a central minimum in both spectral regions and are consistent with the central luminosity 'spike' of M87 being completely non-thermal. The coefficients $h_3,\ldots h_6$ are close to zero at all radii. The velocity dispersion rises from ~ 270 km s^{-1} at ~ 15 arcsec to ~ 305 km s^{-1} at ~ 5 arcsec, and then to ~ 400 km s^{-1} at 0.5 arcsec.

We model the observed velocity dispersions by solving the Jeans equation for hydrostatic equilibrium. Radial anisotropy ($\beta \approx 0.5$) is required in the outer parts to fit the observed velocity dispersion gradient. Near the centre, the data can still be fitted equally well with radially anisotropic models without a central black hole as they can be with less anisotropic models with a central black hole of mass $M_{\rm BH} \lesssim 5 \times 10^9$ M$_\odot$. However, the radially anisotropic Jeans models without a central black hole need not necessarily correspond to a positive and stable distribution function.

We study the central velocity profile of isotropic dynamical models with a central black hole. The wings of the velocity profile are more extended than those of a Gaussian. This is due to the stars that orbit close to the hole at high velocities. The wings contribute significantly to the normalization and the dispersion of the velocity profile. A Gaussian fit to the velocity profile is insensitive to the wings, and thus underestimates both the line strength γ and the velocity dispersion σ. In the analysis of real data, this effect is even more pronounced, since low-frequency information is lost due to continuum subtraction. If M87 has a 5×10^9 M$_\odot$ black hole, we show that for our observational setup, the central line strength will be underestimated by ~ 2 per cent and the central velocity dispersion by ~ 8 per cent. Our blue data show two puzzling features, seen also in the data of other authors: the central line strength is too small to be accounted for solely by the dilution from non-thermal light, and the velocity dispersion in the centre is ~ 30 km s^{-1} smaller than that at $R \approx 0.5$ arcsec. The presence of a central black hole can provide a qualitative explanation for both features.

In addition to the stellar kinematics, we also determine the ionized gas kinematics from the data, by analysing the Hγ emission line. The central velocity dispersion of the ionized gas is very high at ~ 516 km s^{-1}, and drops steeply to ~ 125 km s^{-1} at $R = 2$ arcsec. Interpretation of the ionized gas kinematics in terms of a naive isotropic hydrostatic equilibrium model implies the presence of a central black hole of mass $M_{\rm BH} \approx 3 \times 10^9$ M$_\odot$.

Key words: black hole physics – line: profiles – galaxies: individual: M87 – galaxies: kinematics and dynamics.

★Present address: Institute for Advanced Study, Princeton, NJ 08540, USA.

1 INTRODUCTION

The present paper is the third in a series on the line-of-sight velocity distributions, i.e. the *velocity profiles* (VPs) of galaxies with claimed central black holes. In the first paper (van der Marel et al. 1994a; hereafter Paper I), we reported VP measurements for M31, M32, NGC 3115 and NGC 4594, using the techniques of Rix & White (1992) and van der Marel & Franx (1993; hereafter vdMF). In the second paper (van der Marel et al. 1994b; hereafter Paper II), we constructed detailed axisymmetric models for our data on the E3 galaxy M32, and demonstrated that much new information can be obtained by measuring and modelling deviations of VP shapes from a Gaussian. Here, we present new observations, VP determinations and models for the E0/E1 galaxy M87 (=NGC 4486), which is located in the centre of the Virgo cluster and is a prime candidate to contain a massive central black hole. It is an extended radio source, its nucleus emits non-thermal emission over a long range of wavelengths, and, most strikingly, it has an optical synchrotron jet (e.g. Biretta, Stern & Harris 1991).

Models for the growth of a black hole in a galactic nucleus predict the presence of a central power-law cusp in the mass density (Bahcall & Wolf 1976; Young 1980). Young et al. (1978) detected the presence of starlight emission near the centre of M87, in excess of that expected for an isothermal core, and interpreted this in terms of a model with an $M_{\rm BH}=2.6\times10^9\,{\rm M}_\odot$ black hole. *HST* observations have recently confirmed that M87 indeed does not have a constant surface brightness core, but has a central cusp of the form $I(R)\propto R^{-0.26}$ for $R\leq3$ arcsec (Lauer et al. 1992; Crane et al. 1993). This is consistent with, but does not necessarily imply, the presence of a central black hole (Kormendy 1993). Kinematical evidence is required to demonstrate its presence beyond doubt.

Simultaneously with the photometric observations of Young et al. (1978), Sargent et al. (1978) presented kinematical observations that revealed an increase in the velocity dispersion, going from $R=10$ to 1.5 arcsec. They showed that this implies the presence of a $5\times10^9\,{\rm M}_\odot$ black hole, if the stars have an isotropic velocity distribution. Unfortunately, there is no physical reason why this should be so. In the past decade, many authors have shown that radially anisotropic models without a central black hole can fit the data just as well as isotropic models with a central black hole (Duncan & Wheeler 1980; Binney & Mamon 1992; Newton & Binney 1984; Richstone & Tremaine 1985; Dejonghe 1989; Dressler & Richstone 1990), although these models might not be stable (Merritt 1987). Dressler & Richstone concluded that their data exclude a black hole more massive than $4\times10^9\,{\rm M}_\odot$.

Apart from the interpretation of the spectroscopic data, the data itself have also remained controversial. Although the most recent studies of the blue and green region of the spectrum (Dressler & Richstone 1990; Jarvis & Peletier 1991) agree that the central velocity dispersion of M87 is $\lesssim400$ km s^{-1}, Jarvis & Melnick (1991) recently claimed, from observations of the IR Ca II triplet region, that the central velocity dispersion of M87 is as high as ~460 km s^{-1}. Jarvis & Melnick also raised doubts as to the nature of the central 'luminosity spike' (i.e. the optical point source) in the centre of M87. Studies in the blue and green region of the spectrum all agree that its light must be non-thermal (synchrotron) emission (Dressler & Richstone 1990; Carter & Jenkins 1992; Kormendy 1992). Jarvis & Melnick (1991) detected no central decrease in the strength of the IR Ca II triplet lines, and hence concluded that in the IR there is no dilution from a non-thermal continuum. They also claimed to have resolved the central luminosity spike of M87 (which *HST* has shown to be incorrect) and interpreted it as a massive young star cluster.

In this paper, we present new, high signal-to-noise ratio (S/N), subarcsec resolution spectra of M87, obtained simultaneously in the spectral regions around the blue G-band and the IR Ca II triplet. We use the absorption line spectra to determine the stellar kinematics and VPs, and we use the Hγ emission line in our blue spectra to study the kinematics of the ionized gas near the centre of M87. We solve the Jeans equation of hydrostatic equilibrium, in order to study the constraints that the stellar and ionized gas kinematics put on the presence and mass of a central black hole. In addition, we make a study of the central VP of models with a central black hole. Bahcall & Wolf (1976) already demonstrated that such VPs have wings that are more extended than those of a Gaussian. This is due to the stars that orbit close to the hole at very high velocities. The central VP deviates more from a Gaussian shape for models with a larger black hole mass and for observations of higher spatial resolution. In spite of the results of Bahcall & Wolf, it has been common practice to fit Gaussian VPs to observed galaxy spectra, even for galaxies with suspected black holes. Now that it has become possible to determine VP shapes from data, it is more than justified to readdress this issue. In the present paper, we discuss the VPs of models with a central black hole in the context of our own data. In another paper (van der Marel 1994), we discuss the VPs that are to be expected with the much higher spatial resolution of the *HST*.

The paper is organized as follows. In Section 2, we discuss the observations and the data. In Section 3, we model the observed intensity profile along the slit by comparing it to the available *HST* photometry. In Section 4, we determine the spectrum of the central luminosity spike and the emission-line gas. In Section 5, we determine and discuss the line strengths, the stellar kinematics and VP shapes. In Section 6, we use the Jeans equation to model the stellar kinematics. In Section 7, we calculate and discuss the VPs of isotropic models with a central black hole. In Section 8, we discuss distribution functions of anisotropic models for the M87 stellar kinematics. The ionized gas kinematics are determined in Section 9 and modelled in Section 10. Conclusions are presented in Section 11.

2 SPECTROSCOPIC OBSERVATIONS

Long-slit spectroscopic observations of M87 were obtained in 1992 May 19–22 with the ISIS double-beam spectrograph on the 4.2-m William Herschel Telescope (WHT) on La Palma. Spectra were taken around the blue G-band (~4300 Å) and the IR Ca II triplet (8498.06, 8542.14, 8662.17 Å), using the blue and the red arm of the spectrograph, respectively. Table 1 lists the instrumental setups. Other data from the same observing run (for NGC 3115 and 4594) were presented in Paper I.

Table 1. Instrumental and observational setups.

Telescope	WHT	WHT
Spectrograph	ISIS (Blue)	ISIS (Red)
λ range (Å)	4215-4615	8390-8820
slit position angle (degrees)	65	65
total exposure time (minutes)	180	240
seeing FWHM (″)[a]	0.79	0.63
scale (″/pix)	0.36	0.34
slit width (″)	1.0	1.0
$\sigma_{\rm instr}$ (km s^{-1})[b]	23	10
Dispersion (Å/pix)	0.37	0.37
Grating (lines/mm)	1200	1200
Detector	Tek. CCD (TK1024)	EEV CCD (P88200)
gain (e$^-$/ADU)	2.4	0.8
readout noise (e$^-$/pix)	15	3.8

[a]The PSF is given by equation (1).
[b]The spectral resolution for the given slit width. Listed is the Gaussian dispersion of the spectral lines in the arc lamp frames.

A total of 3 h of data were obtained with both arms of the spectrograph simultaneously, and an additional hour was obtained with the red arm only. The galaxy observations consisted of individual exposures of 30 min. At the beginning of each exposure, the galaxy was centred on the slit by hand (accurate to ~0.1–0.2 arcsec), using a TV camera. During each exposure, guiding was done with an off-axis imaging autoguider. Exposures of arc lamps were taken in between galaxy exposures. The data reduction was done as described in section 2 of Paper I. Standard steps included: bias subtraction, flat-fielding, cosmic ray removal, wavelength calibration, logarithmic wavelength rebinning, rebinning to correct for S-distortion, sky subtraction and dark-current subtraction. The wavelength dependence of the efficiency of the telescope–detector combination was corrected, based on observations of the spectrophotometric standard star BD+17°4708 (Oke & Gunn 1983). Individual galaxy exposures were reduced separately and then added later to yield a single two-dimensional spectrum for each spectral region. Stellar spectra were taken during twilight, for use as templates in the kinematical analysis (see Section 5.1).

A slit position angle PA=65° was used, close to the parallactic angle at the time of the observations. This minimizes the effects of differential atmospheric refraction on the placement of the slit. The average offset of the slit from the galaxy centre can be calculated using the known refractive properties of the earth's atmosphere. The offsets, (0.11 ± 0.05) arcsec for the blue spectra and (0.02 ± 0.01) arcsec for the IR spectra, are very small, and will henceforth be neglected. The adopted slit position angle corresponds roughly to the minor axis for radii $\gtrsim 30$ arcsec (Peletier et al. 1990). At smaller radii, M87 shows significant isophote twisting (Lauer et al. 1992). The slit position angle is far from that of the optical jet of M87, which has PA=292°.5.

Fig. 1 shows the blue and IR sky spectra, template spectra and galaxy spectra at various galactocentric distances. The template spectra are weighted sums of individual stellar spectra, as described in Section 5.1. The galaxy spectra have high S/N (e.g. at $R=0$ arcsec: 100 per Å for the blue spectrum and 70 per Å for the IR spectrum). The spectral resolution of the data is much higher than that which is typically used for studies of galaxy spectra. Both the instrumental velocity dispersion and the velocity scale per pixel (see Table 1) are much smaller than the velocity dispersion of the stars in M87 ($\gtrsim 250$ km s^{-1}). The absorption lines in the galaxy spectra are redshifted with respect to those in the template spectra, due to the systemic velocity of M87. The blue spectrum shows a large number of both weak and strong absorption lines, whereas the IR spectrum is dominated by the three Ca II triplet lines. The emission lines in the galaxy spectra will be discussed in Section 4 (see Fig. 3). There are many bright sky lines at the IR wavelengths. These are difficult to subtract, which is especially evident from the spectra at large galactocentric distances. In the kinematical analysis of Section 5, emission lines and bright sky lines are masked, using the masks displayed at the top of the panels in Fig. 1.

3 INTENSITY PROFILE MODELLING

For each spectral region, the observed intensity profile along the slit can be modelled by convolving high spatial resolution *HST* photometry of M87 with a seeing point-spread-function (PSF), integrating the result over the width of the slit, and binning it into pixels of the appropriate size. This allows a *post hoc* determination of the seeing FWHM of the spectroscopic observations.

To model the intensity profiles, one needs B-band photometry for the blue spectra and I-band photometry for the IR spectra. The observed wavelength ranges for our spectra (see Table 1) are near the centres of these photometric bands (the photometric B band has $\lambda_0\approx 4400$ Å and $[\Delta\lambda]_{\rm FWHM}\approx 1000$ Å, and the photometric I band has $\lambda_0\approx 8800$ Å and $[\Delta\lambda]_{\rm FWHM}\approx 2400$ Å). *HST* I-band photometry was published by Lauer et al. (1992). B-band photometry is obtained by assuming $(B-I)_{\rm sp}=1.60$ mag and $(B-I)_*=2.75$ mag, for the colours of the central luminosity spike and the starlight, respectively. These values follow from $(B-V)_{\rm sp}=0.87$ mag, $(B-V)_*=1.02$ mag (Young et al. 1978), $(V-I)_{\rm sp}=0.73$ mag and $(V-I)_*=1.73$ mag (Lauer et al. 1992).

In Paper I, it was found that the *shape* of the PSF for our spectroscopic observations can be well described by a sum of two Gaussians:

$$\mathrm{PSF}(R)=A_1 e^{-R^2/2\sigma_1^2}+A_2 e^{-R^2/2\sigma_2^2}, \qquad (1)$$

with fixed ratios of the dispersions, $\sigma_2/\sigma_1=2.40$, and amplitudes, $A_2/A_1=0.13$, of the two components. The PSF is normalized for $A_1=0.091\,01/\sigma_1^2$, and is fully specified by its FWHM $S=2.521\,30\,\sigma_1$.

The best fits of the convolved *HST* photometry (including the central $R^{-0.26}$ surface brightness cusp) to the observed intensity profiles along the slit were obtained with $S=0.79$ arcsec for the blue spectra and $S=0.63$ arcsec for the IR spectra. The observed intensity profiles and the fits are displayed in Fig. 2. Also shown are the individual contributions of the starlight and the central luminosity spike to the observed intensity in each pixel. The spike is bluer than the starlight, and thus contributes more to the blue spectrum than to the IR spectrum.

The values of the seeing FWHM thus obtained are consistent with estimates of the size of the seeing disc provided

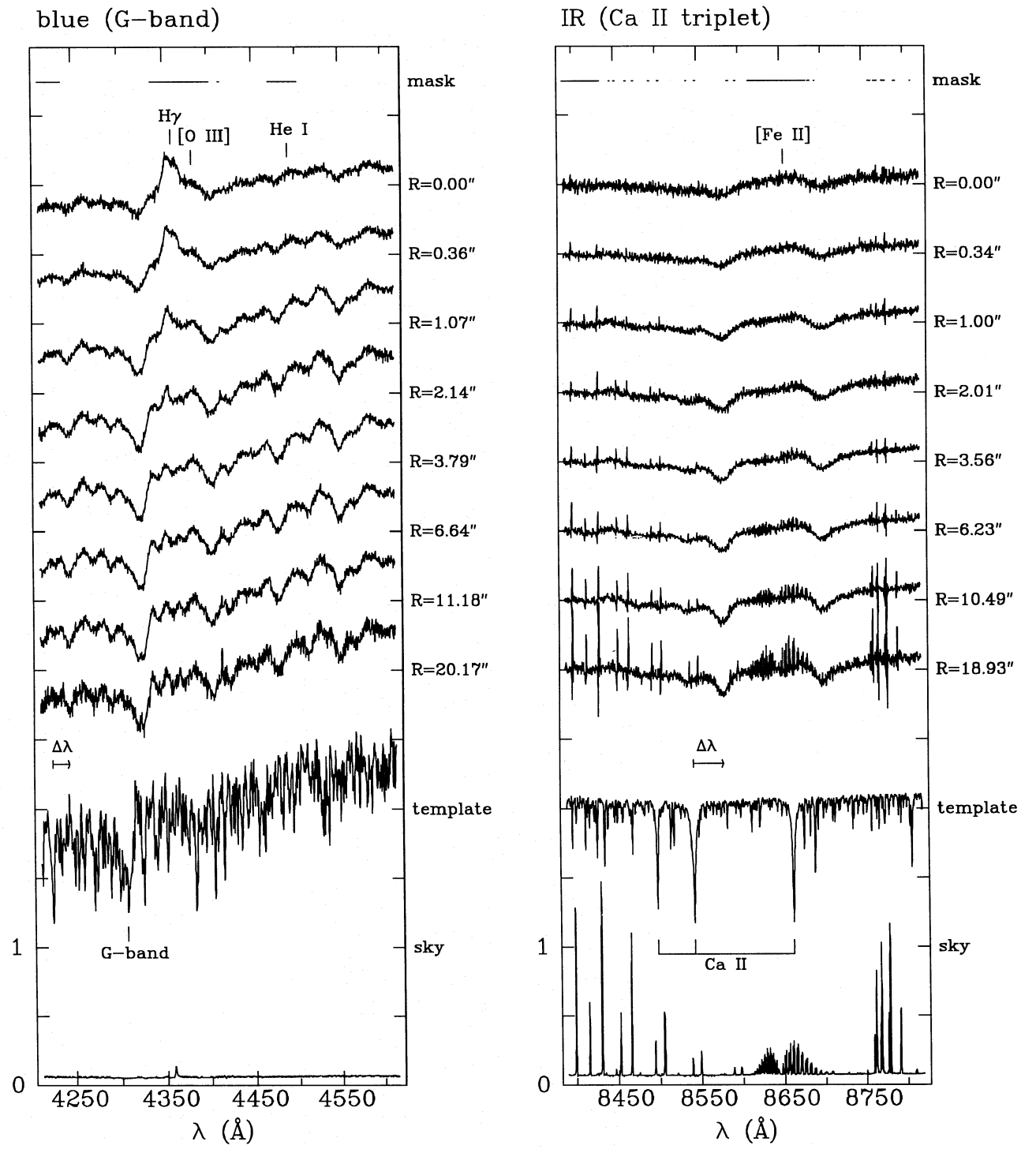

Figure 1. Schematic representation of the data. M87 spectra are shown for various galactocentric distances. For the purpose of this figure, the data were rebinned in the spatial direction, and data at opposite sides of the galaxy centre were averaged (M87 has negligible rotation). The template spectrum is a weighted sum of individual stellar spectra, as described in Section 5.1. The galaxy and template spectra are sky-subtracted and normalized to a mean of 1. The plotted sky spectrum is the observed sky spectrum divided by the mean flux in the central galaxy spectrum. For each spectrum, unity is at the height of the label in the right margin and zero is two tick marks below that. The emission lines are discussed in Section 4. The mask at the top of each panel shows the pixels that were excluded from the fit when determining the stellar kinematics (see Section 5). The wavelength scale is logarithmic, but this is hardly noticeable as a result of the small spectral range of each data set.

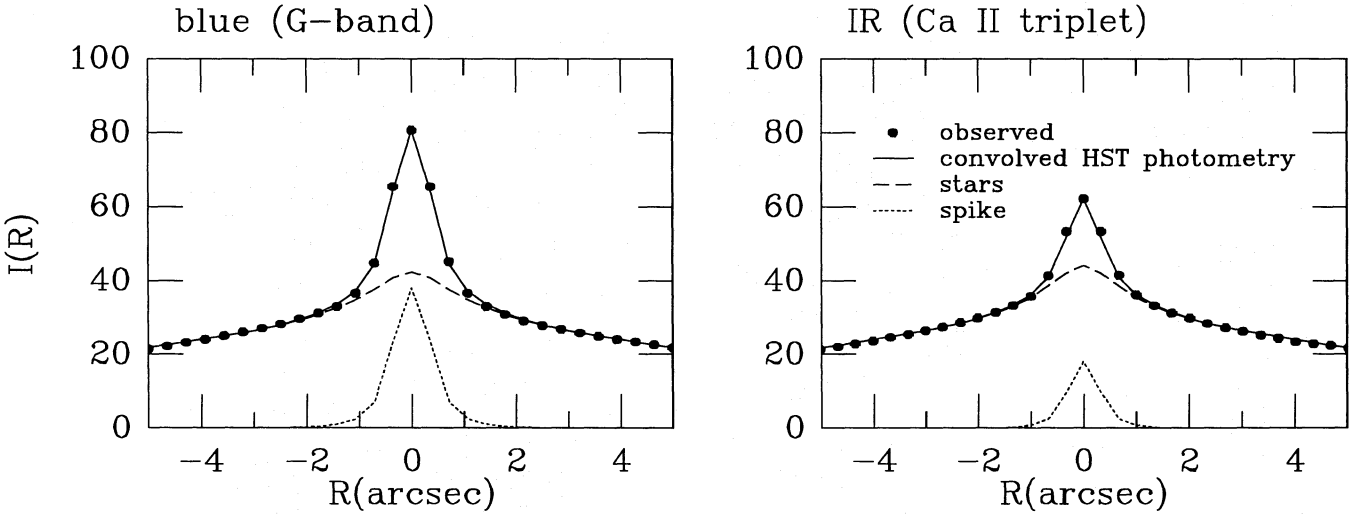

Figure 2. The dots show the observed intensity profiles along the slit for our blue and IR spectra. The solid curves are predicted profiles, obtained by convolving the *HST* photometry of Lauer et al. (1992) with seeing PSFs of the form of equation (1), with FWHM $S = 0.79$ and 0.63 arcsec, respectively, and rebinning according to our observational setup. The fits to the data are excellent. The dashed and dotted curves show the individual contributions of the starlight and the central luminosity spike to the total intensity observed in each pixel. The vertical scale is in arbitrary units.

by the autoguider of the telescope during the observations. The seeing is larger in the blue than in the IR, consistent with the dependence of seeing on wavelength expected on theoretical grounds (e.g. Léna 1988). The seeing of our observations is better than that of previous studies of the kinematics of the stars and gas in M87. The small pixel size in the spatial direction (see Table 1) is essential to exploit fully these excellent subarcsecond seeing conditions. A slit width of 1 arcsec was used to obtain high S/N, whilst not sacrificing too much spatial resolution.

4 THE SPECTRUM OF THE CENTRAL LUMINOSITY SPIKE AND THE EMISSION-LINE GAS

Fig. 3 shows the galaxy spectrum for the 'nuclear' region $|r| \leq 0.5$ arcsec, for both observed wavelength ranges. To obtain the contributions of the central luminosity spike and emission-line gas to these spectra, one must subtract the spectrum of the starlight. We estimate this starlight spectrum by averaging the data in the 'extra-nuclear' region between 3 and 5 arcsec. In this region, the emission from the pronounced Hγ line has become undetectable (cf. Fig. 1), and the contribution of the central luminosity spike has become negligible (cf. Fig. 2). The velocity dispersions for the two regions, $\sigma_{\rm nuc}$ and $\sigma_{\rm exnuc}$, were estimated using the techniques described in Section 5. The extranuclear spectrum was then convolved with a Gaussian of dispersion $(\sigma^2_{\rm nuc} - \sigma^2_{\rm exnuc})^{1/2}$, to make its velocity dispersion identical to that of the nuclear spectrum. Subsequently, the extranuclear spectrum was normalized to the expected starlight normalization for the nuclear spectrum, using the results of Fig. 2. Upon subtraction from the nuclear spectrum, one then obtains an estimate for the spectrum of the central luminosity spike and the emission-line gas, as displayed in Fig. 3. Our approach is similar to that used by several other authors, but more detailed in that it: (i) takes into account the $R^{-0.26}$ surface brightness cusp of M87, and (ii) corrects for variations in the velocity dispersion as a function of radius.

The starlight-subtracted nuclear spectra show no sign of absorption lines. This indicates that the central luminosity spike in M87 is non-thermal, both in the blue and in the IR. For the blue region of the spectrum, this is consistent with the findings of Dressler & Richstone (1990), Kormendy (1992) and Carter & Jenkins (1992). For the IR region, a similar analysis has not been presented before, but Jarvis & Melnick (1991) claimed the central luminosity spike to be *thermal*, based on IR line strength measurements. The nature of the central luminosity spike will be addressed further in Section 5.4.

The starlight-subtracted nuclear spectrum was fitted with a polynomial to estimate the non-thermal continuum. This fit was then subtracted to yield an estimate for the spectrum of the emission-line gas. Three emission lines could be identified in the blue spectrum: Hγ (4340.47 Å), [O III] (4363.21 Å) and He I (4471.50 Å). In the IR spectrum, we (marginally) detect [Fe II] (8616.96 Å). We fitted a Gaussian to each of these lines, yielding the results displayed in the lower panels of Fig. 3. All four lines (and many more) have also been detected in the H II region NGC 1976 (the Orion nebula; Osterbrock, Tran & Veilleux 1992). The flux ratios of the lines in our blue spectrum are $F([{\rm O\,III}])/F({\rm H}\gamma) = 0.06 \pm 0.02$ and $F({\rm He\,I})/F({\rm H}\gamma) = 0.17 \pm 0.02$. For the Orion nebula, these ratios are $F([{\rm O\,III}])/F({\rm H}\gamma) = 0.031$ and $F({\rm He\,I})/F({\rm H}\gamma) = 0.105$. The IR [Fe II] line has been seen in other active galaxies as well (Malkan & Filippenko 1983), and was also detected by Jarvis & Melnick (1991) in their study of the IR spectrum of M87. The emission lines in the region 4900–7300 Å were described by Boroson & Thompson (1991).

The vertical bars in the lower panels of Fig. 3 indicate the expected positions of the emission lines, if the gas were to

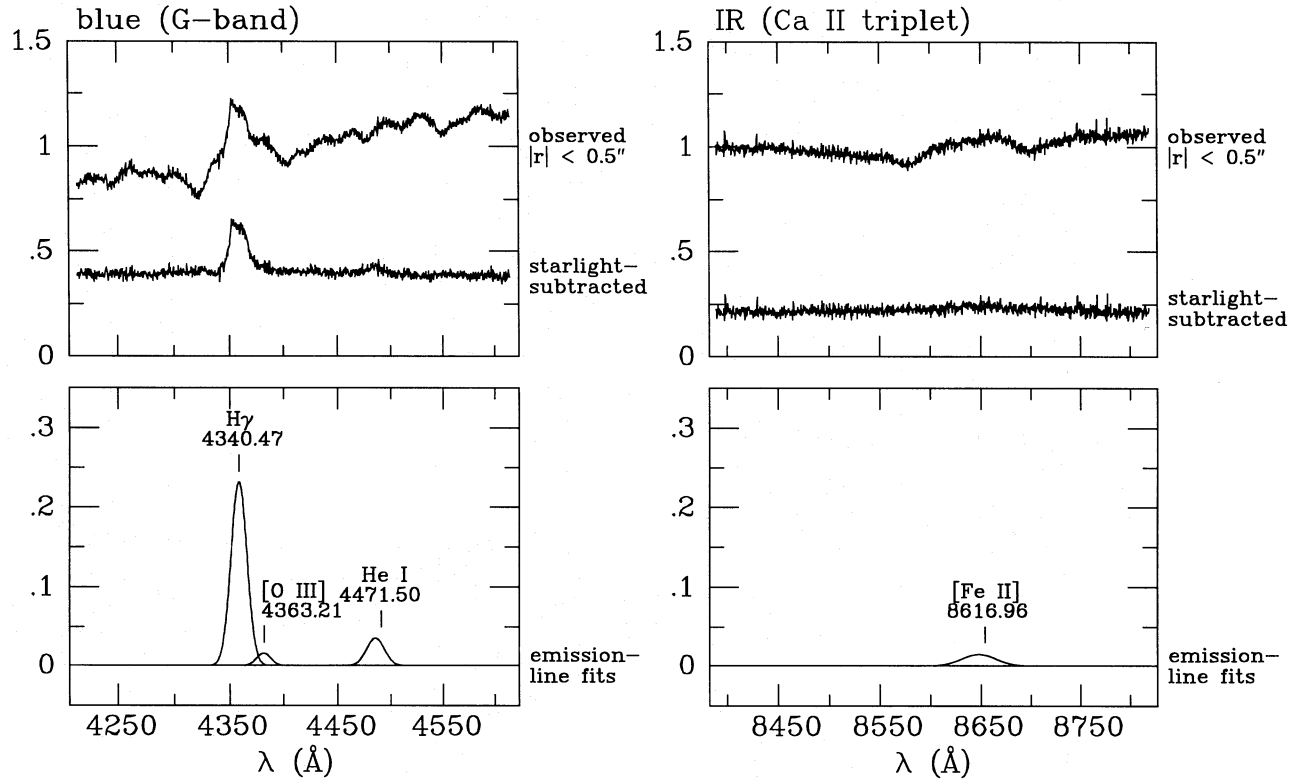

Figure 3. The top panels show two spectra for each spectral region. The top spectrum is the total (sky-subtracted) galaxy spectrum in the central three pixels, normalized to unity. The lower spectrum is obtained after subtracting the starlight contribution. This yields the combined contribution of the central luminosity spike and emission-line gas. The light from the spike is entirely non-thermal. After subtraction of the non-thermal continuum, four emission lines could be detected. The lower panels show Gaussian fits to these lines. The vertical bars indicate the expected positions if the gas were to move at the systemic velocity. Note the change in the vertical scale between the upper and the lower panels.

move at the systemic velocity (to be determined in Section 5.3). The He I and the [Fe II] lines are blueshifted with respect to the systemic velocity. The velocity dispersion of the Hγ line is $\sigma = 501 \pm 9$ km s^{-1} (for $|r| \leq 0.5$ arcsec). The dispersions of the other lines are all consistent with this value: $\sigma = 436 \pm 114$ km s^{-1} for the [O III] line, $\sigma = 555 \pm 45$ km s^{-1} for the He I line and $\sigma = 590 \pm 98$ km s^{-1} for the [Fe II] line. In Section 9, we study the kinematics of the Hγ line as a function of position along the slit.

5 STELLAR KINEMATICS

5.1 Method of analysis

Emission lines and ill-subtracted sky lines must be masked when fitting to the observed galaxy spectra. This is straightforward when the fitting is done in pixel space, but complicated when it is done in Fourier space (as in, for example, the method used by vdMF). Methods for fitting galaxy spectra in pixel space were recently developed by Rix & White (1992), Kuijken & Merrifield (1993) and Saha & Williams (1994). In Paper I, we used the method of Rix & White. Here we use yet another method, described in detail in Appendix A. We convolve a template spectrum with parametrized VPs, and, for any set of parameters, we define a χ^2 quantity by direct comparison to the galaxy spectrum. By minimizing this χ^2, we obtain the best-fitting parameters and their formal errors. The method uses 'brute force' and is not dissimilar to the techniques used many years ago, by, for example, Burbidge, Burbidge & Fish (1961) and Richstone & Sargent (1972). It is not as versatile and sophisticated as some of the other methods for solving the pixel space fitting problem, but it is conceptually straightforward and relatively easy to program. It has the additional advantage that essentially any observational effect can be easily incorporated or corrected for.

We use the same approach as in vdMF and Paper I, by parametrizing the VP as a Gauss–Hermite series and fitting VPs of the form

$$\mathscr{L}(v) = \frac{1}{\sigma}\alpha(w)\left[1 + \sum_{j=3}^{N} h_j H_j(w)\right],$$

$$w \equiv (v - V)/\sigma, \qquad \alpha(w) = \frac{1}{\sqrt{2\pi}} e^{-(1/2)w^2} \tag{2}$$

to the data. The functions H_l are the Hermite polynomials given in appendix A of vdMF. The parameters V and σ are the mean and dispersion of the best-fitting Gaussian VP to the data. The Gauss–Hermite moments $h_3, \ldots h_6$ measure deviations of the VP from the best-fitting Gaussian. For 'ideal data' they satisfy

$$h_l = (2\sqrt{\pi})\frac{\gamma_0}{\gamma}\int_{-\infty}^{\infty} \mathscr{L}_0(v)\,\alpha(w)\,H_l(w)\,\mathrm{d}v, \tag{3}$$

where $\mathscr{L}_0(v)$ is the true line-of-sight velocity distribution of the galaxy, γ_0 measures the ratio of the equivalent width of the absorption lines in the galaxy and the template spectrum, and γ is the estimate for the 'line strength' obtained from the data. Differences in equivalent width can arise through differences in the spectral type (spectral mix) or metallicity of the galaxy and template spectra, or through a contribution of a non-thermal (line-less) continuum in the galaxy spectrum. The line strength parameter is a global correction factor rather than a well-defined physical quantity, because the physical mechanisms that determine the strength of individual absorption lines in stellar atmospheres are different for different lines.

The short-wavelength end of each spectral range (where there is no template information available to compare with the galaxy data) and regions around sky lines, emission lines and bad columns were masked when fitting the galaxy data. Masked pixels were excluded from the calculation of the quantity χ^2 in equation (A9). The masks are displayed at the top of Fig. 1. In each spectral region, the mask contains $\sim 1/3$ of the total number of pixels.

Differences in continuum shape between the galaxy and template spectrum are modelled as a polynomial of order L (cf. equation A2). Unsatisfactory results (i.e. large χ^2 values) were obtained with $L=1$ and $L=2$. Kinematical quantities obtained with $L=3$, 4, 5 or 6 were found to be nearly indistinguishable. To obtain the results discussed below, we used $L=3$.

We construct template spectra for the analysis as weighted sums of individual stellar spectra (see Appendix A3; a similar approach was used by Rix & White 1992). During our observing run, stellar spectra were observed of giant stars (Morgan–Keenan luminosity class III) of spectral types G5, G8, K0 (2x), K2 (2x), K3, K5 and M0, subdwarfs (MK class IV) of spectral types G5, G8 and K2, and dwarfs (MK class V) of spectral types G0, G5, K1, K7 and M0. The best-fitting template spectrum for M87 was determined by fitting to the total galaxy spectrum between 3 and 6 arcsec from the centre. For the blue spectral region, the best-fitting stellar mix consists of a K1 V star (44 per cent), a K2 III star (40 per cent), a G5 IV star (13 per cent) and an M0 V star (3 per cent). For the IR spectral region, the best-fitting stellar mix consists of an M0 III star (90 per cent), a K2 III star (9 per cent) and a G5 III star (1 per cent). The best-fitting template spectrum for each spectral region is displayed in Fig. 1. The inferred template mixes serve merely to avoid errors in the kinematical analysis. None the less, the mix we obtain for the blue spectrum is not dissimilar to that indicated by stellar population synthesis models for elliptical galaxies (Pickles 1985b). The inferred mix for the IR spectra is discussed at the end of Section 5.5.

We also determined the best-fitting template mix, using data at other galactocentric distances. However, the template mix was found to be similar in each case. In the final analysis of the galaxy data, we therefore adopted the same template mix for each available galaxy spectrum, rather than fitting a different template at each distance. The line strength parameter γ *is* allowed to vary as a function of distance, so possible stellar population gradients can still be accounted for.

In the final analysis, the galaxy data were rebinned spatially, to yield an approximately constant S/N. No rebinning was applied in the inner 3 arcsec. Similar rebinning was applied to the blue and IR spectra. This yields a higher S/N for the IR data than for the blue data. None the less, the formal errors on the quantities derived from the IR data are larger than those derived from the blue data, because the blue region of the spectrum has more strong absorption lines. The inferred VP parameters for each spectral region are displayed in Figs 4(a) and (b). Tables of the results are given in Appendix C. Positive radii lie in the direction of the position angle listed in Table 1.

5.2 Deviations from Gaussian velocity profiles

The Gauss–Hermite coefficients derived from the data all scatter around zero. For each coefficient and spectral region, we calculated the (weighted) averages $\langle h_l\rangle_+$ and $\langle h_l\rangle_-$ of the coefficients at positive and negative radii, respectively. As in Paper I, we define quantities

$$\langle h_l\rangle_e \equiv \frac{1}{2}(\langle h_l\rangle_+ + \langle h_l\rangle_-), \qquad \langle h_l\rangle_o \equiv \frac{1}{2}(\langle h_l\rangle_+ - \langle h_l\rangle_-) \tag{4}$$

('e' for 'even', 'o' for 'odd'). These quantities are listed in Table 2. For an equilibrium stellar system, h_l must be an even function of radius for even l, and an odd function for odd l. For such a stellar system, $\langle h_3\rangle_o$, $\langle h_4\rangle_e$, $\langle h_5\rangle_o$ and $\langle h_6\rangle_e$ thus measure average deviations of the VP from a Gaussian, whereas $\langle h_3\rangle_e$, $\langle h_4\rangle_o$, $\langle h_5\rangle_e$ and $\langle h_6\rangle_o$ measure systematic errors in the analysis. The former quantities are all consistent with zero to within 1 per cent. This suggests that our coefficients γ, V and σ in Figs 4(a) and (b) (which were obtained by fitting Gaussian VPs to the data) are good estimates of the true line strength, mean velocity and velocity dispersion. We will argue, however, in Section 7, that this might not be the case if M87 indeed has a massive central black hole.

5.3 Mean velocities

The average of the mean heliocentric velocities outside 5 arcsec is 1283.2 ± 2.6 km s^{-1} for the blue G-band data and 1271.6 ± 2.8 km s^{-1} for the IR Ca II triplet data. Figs 4(a) and (b) show the residuals with respect to these mean values. The difference between the two mean values is most likely the result of some unidentified systematic error. Henceforth we assume a heliocentric systemic velocity of 1277.4 km s^{-1}, which is the average of the values for the two spectral ranges. This value agrees with the velocity of 1282 ± 9 km s^{-1} given by the RC3 (de Vaucouleurs et al. 1991).

The averages of the mean heliocentric velocities at positive and negative radii agree to within 5 km s^{-1}, both for the blue and the IR data. M87 thus has no velocity gradient (i.e. rotation) along the slit position angle PA = 65° of our observations. This is consistent with some, but not all, previously published results. Sargent et al. (1978) and Jarvis & Melnick (1991) found no rotation along PA = 90°. Davies & Birkinshaw (1988) found some evidence for rotation with amplitude $V_{max} \approx 30$ km s^{-1} along PA = 80°, but no evidence for rotation along PA = 50°. Jarvis & Peletier (1991) found evidence for rotation with amplitude $V_{max} \approx 15$ km s^{-1} along PA = 60°.

Our blue and IR spectra both indicate that the mean velocity of the centre of M87 is ~ 40 km s^{-1} smaller than the inferred systemic velocity. This was also seen by Dressler &

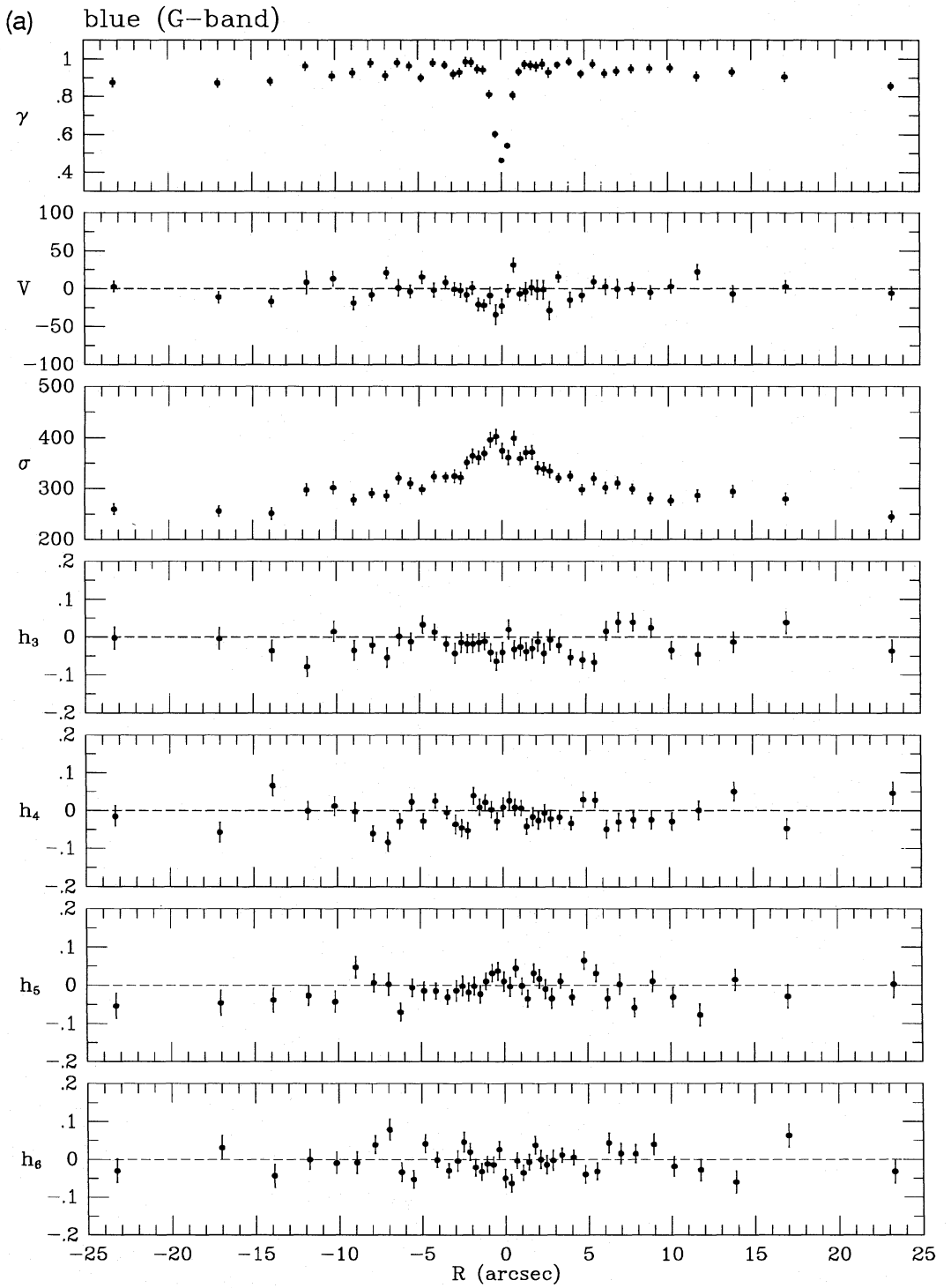

Figure 4. (a) The line strength γ, mean velocity V, velocity dispersion σ and Gauss–Hermite moments $h_3, \ldots h_6$, as determined from the blue G-band data. The quantities V and σ are in km s^{-1}. (b) As (a), but for the IR Ca II triplet data.

Richstone (1990). By contrast, Jarvis & Peletier (1991) claimed that the centre moves at the systemic velocity, but that the velocity of the annulus with 2 arcsec $\lesssim R \lesssim$ 4 arcsec is smaller than the systemic velocity. Jarvis & Melnick (1991) found no velocity anomaly at all. The observed deviations from the systemic velocity might be real, and due possibly to a recent merger (Jarvis & Peletier 1991). Either way, all deviations from the systemic velocity are much smaller than the velocity dispersion of M87, and are thus dynamically insignificant. They will henceforth be neglected.

5.4 Line strengths

Our results show that the line strength γ has a pronounced central minimum in both spectral regions. This confirms previous results of Dressler & Richstone (1990) and Jarvis &

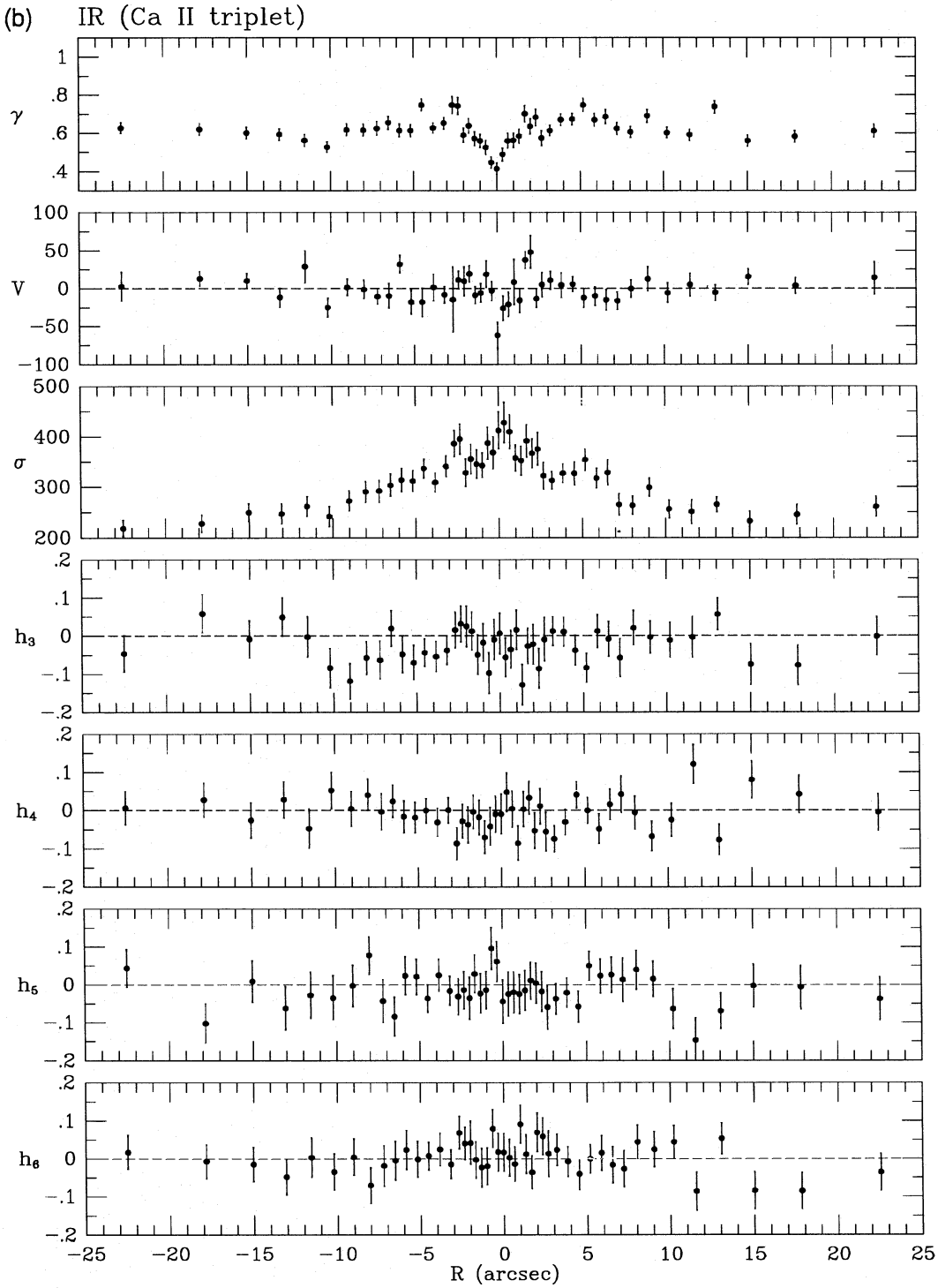

Figure 4. – *continued*

Table 2. Overall characteristics of the Gauss–Hermite coefficients.

spectrum	$\langle h_3\rangle_o$	$\langle h_4\rangle_e$	$\langle h_5\rangle_o$	$\langle h_6\rangle_e$	$\langle h_3\rangle_e$	$\langle h_4\rangle_o$	$\langle h_5\rangle_e$	$\langle h_6\rangle_o$
blue	0.000	-0.009	0.004	-0.006	-0.019	0.000	-0.007	-0.002
IR	0.003	-0.008	-0.004	0.003	-0.024	-0.001	-0.011	-0.001

The listed quantities are defined in equation (4). The formal errors are 0.004 for the blue quantities and 0.007 for the IR quantities. If M87 is assumed to be an equilibrium stellar system, the first four quantities measure average VP deviations from a Gaussian, whereas the last four quantities measure systematic errors in the analysis.

Peletier (1991), concerning the blue and visual parts of the spectrum, but contradicts the claim of Jarvis & Melnick (1991) that the line strength γ does not decrease towards the centre in the IR Ca II triplet region of the spectrum.

Our results in Section 4 indicate that the light from the central luminosity spike in M87 is probably completely non-thermal. This would explain the observed decrease in the line strength towards the centre as being due to dilution by the light from the spike. Our analysis in Section 3 allows us to test this quantitatively. From Fig. 2, we know the fraction f of the total light in each pixel that is due to the central luminosity spike. If this light is non-thermal, the observed line strength $\gamma_{\rm obs}$ at a given position will be

$$\gamma_{\rm obs} = \gamma_{\rm t}(1-f), \qquad (5)$$

where $\gamma_{\rm t}$ is the true line strength of the galaxy's *star*light. Upon assuming a constant value for $\gamma_{\rm t}$ that fits the observed line strengths between 2 and 5 arcsec, this yields the predictions $\gamma_{\rm pr}$ displayed as solid curves in Fig. 5.

The predictions fit the observed line strengths reasonably well in the blue region of the spectrum, except for the points at radii $R=0$ and 0.36 arcsec, where $\gamma_{\rm obs} < \gamma_{\rm pr}$. In the IR region of the spectrum $\gamma_{\rm obs} < \gamma_{\rm pr}$ over the whole region $|R| \lesssim 1.5$ arcsec. These results might indicate that the line strength $\gamma_{\rm t}$ of the starlight in M87 decreases towards the centre due to a change in the stellar population. One would then expect, however, to see discrepancies in Fig. 5 over the same radial ranges for both spectra, which is not the case. So, we consider it more likely that the discrepancies in Fig. 5 are due to systematic errors in either the predicted or the observed line strengths. There is certainly no evidence that part of the light from the central luminosity spike would be stellar, because one would then expect $\gamma_{\rm obs} > \gamma_{\rm pr}$.

Another way to study the differences between the observed and predicted line strengths is to consider the quantity $I_* \equiv I_{\rm obs}\gamma_{\rm obs}/\gamma_{\rm t}$ ($I_{\rm obs}$ being the observed intensity), which is also displayed in Fig. 5. If the line strength of the starlight is constant and the observed line strengths are free from systematic errors, then I_* measures the starlight intensity. It can be compared to the predictions of Fig. 2 (displayed as dashed curves in Fig. 5). For the IR data, the predicted starlight intensity is slightly more centrally peaked than the inferred intensity. This might be due to small errors in our predictions, for example in the assumed magnitude of the spike or the assumed PSF. For the blue data, however, this can never be the whole story. The inferred starlight intensity has a central *minimum*, in contradiction to the monotonic increase in the starlight intensity towards the centre that has been observed with the *HST* (Lauer et al. 1992). The very same thing can be seen in the data of Dressler & Richstone (1990; their fig. 6), who studied the M87 spectrum around the Mg *b* triplet at ~5175 Å. So, for the blue data, we conclude that the discrepancy between the observed and predicted line strengths at $R=0$ and 0.36 arcsec must be due to some systematic error in the data analysis. In Section 7 we discuss a possible explanation. For

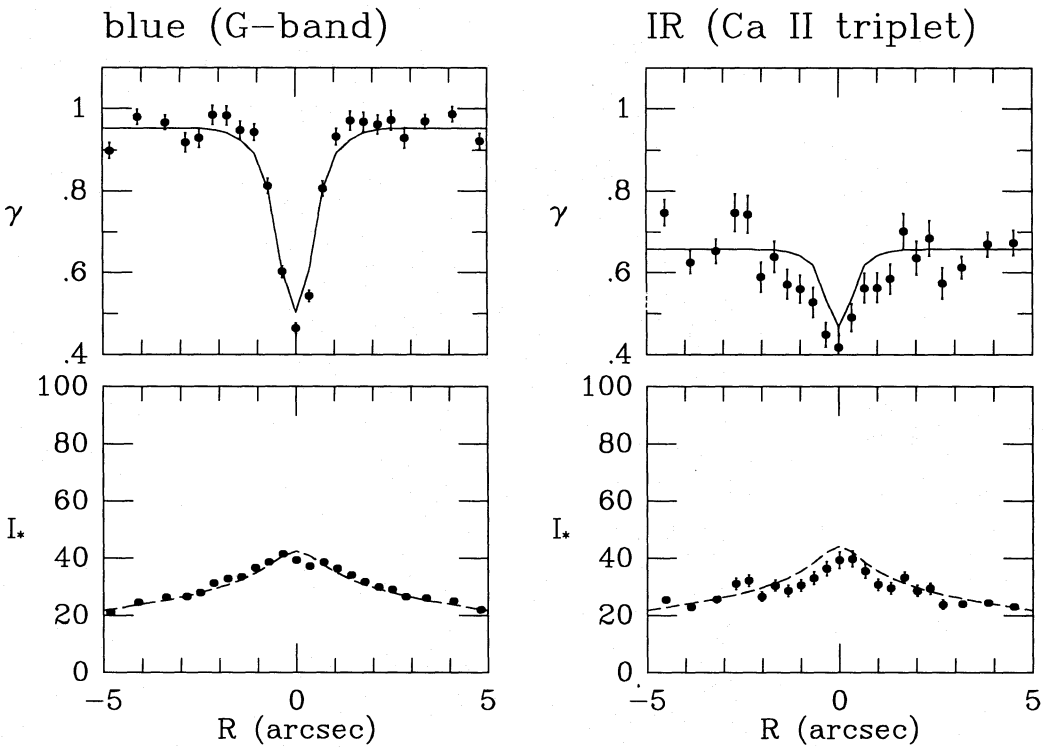

Figure 5. The data points in the two top panels show the line strength γ as in Figs 4(a) and (b). The curves show predictions based on our modelling of Fig. 2 and the assumption that the light from the central luminosity spike in M87 is non-thermal. The data points in the bottom two panels are estimates of the starlight intensity, based on the observed line strengths and total intensities. The dashed curves are the predictions from Fig. 2. The vertical scale in the bottom panels is arbitrary.

the IR data, the discrepancies for $|R| \lesssim 1.5$ arcsec could be the result either of a similar systematic error or of an error in our photometric modelling in Section 2.

The very shallow decrease in the line strength for $R > 5$ arcsec is consistent with the findings of previous authors (e.g. Jarvis & Peletier 1991). It indicates that the metallicity, spectral mix or age of the stellar population changes with radius. This has been studied by many authors, both for M87 and for elliptical galaxies in general (e.g. Pritchet 1977; Peletier 1989; Davies, Sadler & Peletier 1993).

5.5 Velocity dispersions

The velocity dispersions derived from our blue data show a shallow increase from ~270 km s^{-1} at ~15 arcsec to ~305 km s^{-1} at ~5 arcsec. Then the dispersions rise sharply to ~400 km s^{-1} at 0.5 arcsec, followed by a drop to ~370 km s^{-1} in the two pixels at $R = 0$ and 0.36 arcsec. These results are consistent with those of Dressler & Richstone (1990) and Jarvis & Peletier (1991). The latter authors also clearly detected the central decrease in σ. Dressler & Richstone did not see the velocity dispersions rise to values quite as high as 400 km s^{-1} at $R \approx 0.5$ arcsec, but this is most likely a result of the lower spatial resolution of their data.

The absence of a central maximum in σ has previously been used as an argument against the presence of a very massive central black hole in M87. This assumes that the observed central dip in the velocity dispersion is real. However, this does not have to be the case. The radii that represent the dip in the velocity dispersion are suspect because they are the same radii for which the observed line strengths are lower than expected on the basis of the *HST* photometry (see Fig. 5). It is well known that random errors in γ and σ are statistically correlated (e.g. Efstathiou, Ellis & Carter 1980), due to the mathematical properties of a Gaussian (Larsen et al. 1983; vdMF). We show in Section 7 that the presence of a central black hole could cause both the central line strength and the central velocity dispersion to be underestimated.

We do not confirm the result of Jarvis & Melnick (1991) that the velocity dispersion derived from the IR Ca II triplet is constant at ~460 km s^{-1} for $R \lesssim 3$ arcsec. Our velocity dispersions near the centre are ~420 km s^{-1}, and have already fallen below 400 km s^{-1} at $R \approx 0.5$ arcsec. Fig. 6 compares the velocity dispersions derived from our blue spectra to those derived from our IR spectra. The velocity dispersions derived from the IR spectra do not show the central dip seen in the blue results. Between ~0.5 and 10 arcsec, the blue and IR velocity dispersions agree reasonably well, but outside ~10 arcsec the dispersions derived from the blue are ~25 km s^{-1} larger than those derived from the IR data. In spite of these differences, the results derived from the two spectral regions provide a reasonably consistent picture of the structure of M87: the central luminosity spike is non-thermal and the velocity dispersion rises up to ~400 km s^{-1} at $R = 0.5$ arcsec. Closer to the centre, systematic errors might be playing a role.

Our best explanation for the differences between the velocity dispersions derived from the two spectral regions is that there are systematic errors in the IR results. First of all, the smaller equivalent width of the absorption lines in the Ca II triplet region makes it inherently more difficult properly to separate continuum and absorption lines, and hence to determine kinematical quantities (see also Paper I). Secondly, our best-fitting template for the IR data consists mainly (90 per cent) of an M0 giant, the latest stellar type in our template library. This suggests that, in reality, the M87 spectrum might be even later than M0. Stellar population synthesis models do indeed indicate that, in the IR region of the spectrum, a significant fraction of the observed light of elliptical galaxies comes from late-type M5 or M6 stars (e.g. Pickles 1985b). For M stars, the strength and width of the Ca triplet lines are very sensitive functions of the spectral type and metallicity (O'Connell 1973; Cohen 1978; Pickles 1985a). In addition, very broad molecular TiO absorption bands occur in the later M stars (Sharpless 1956). One of these bands lies at 8490 Å, close to one of the Ca II triplet lines. These bands cannot be modelled by any of the stars in our template library, as they occur only in (cool) late-type M stars. Molecular absorption in the Wing–Ford band at ~9916 Å has in fact been detected in M87 (Hardy & Couture 1988). When modelling the observations in the following sections, we will discard the IR results and use only the more accurate blue results.

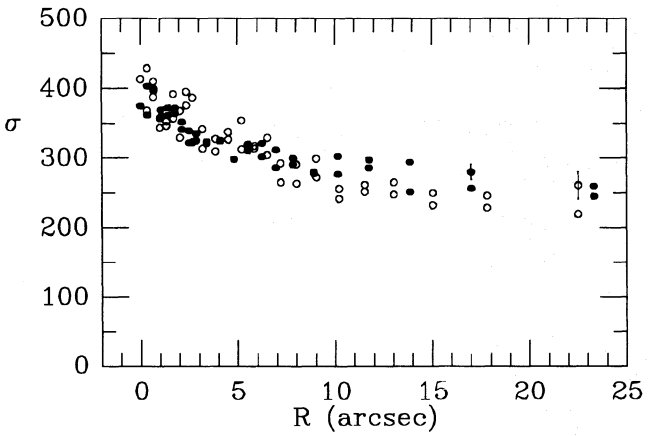

Figure 6. Comparison of the velocity dispersions derived from the blue data (solid dots) and the IR data (open dots). Data points at negative radii were flipped to positive radii. One typical error bar is shown for each data set. On the whole, the results agree well.

6 HYDROSTATIC EQUILIBRIUM MODELS FOR THE STELLAR KINEMATICS

6.1 The luminosity density of M87

To obtain the three-dimensional luminosity density of M87, we need to deproject the observed surface photometry. *HST* *I*-band photometry for $R < 20$ arcsec was published by Lauer et al. (1992). Cousins' R_c band photometry for $R < 163$ arcsec was published by Peletier et al. (1990). Fig. 7 shows the *I*-band surface brightness distribution of M87, as obtained by combining these data sets. For $R < 20$ arcsec we use the Lauer et al. (1992) data, and for $R > 20$ arcsec we use the Peletier et al. (1990) data. The latter data were transformed to the *I*-band using $R_c - I = 1.153$, which is the average colour for 5 arcsec $\lesssim R \lesssim 20$ arcsec. In this region, the two data sets agree well. We neglect the shallow colour gradients in M87. The data were corrected for galactic foreground absorption, assuming $A_I = 0.04$, based on the value of

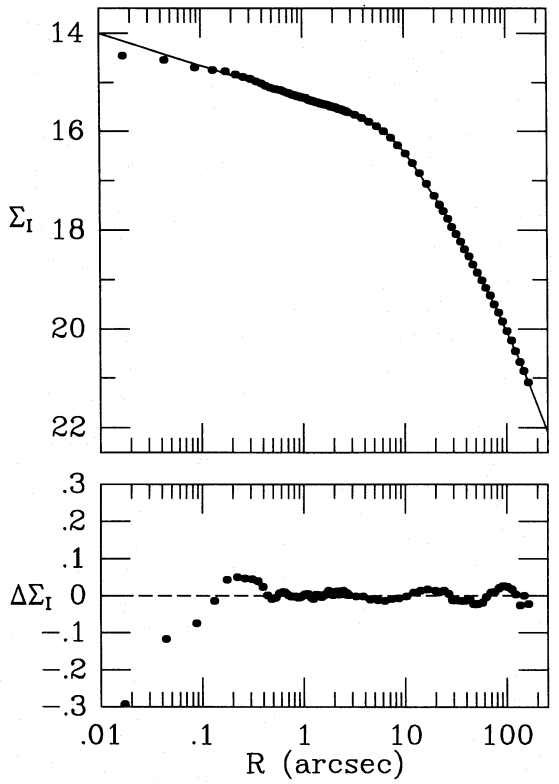

Figure 7. The dots in the top panel show the *I*-band surface brightness profile $\Sigma_I(R)$ in mag arcsec^{-2}, as obtained by combining the data of Lauer et al. (1992) and Peletier et al. (1990). Galactic foreground absorption ($A_I = 0.04$ mag) was corrected for. The curve shows the smooth fit with a central $R^{-0.26}$ cusp given by equation (6). The residuals $\Delta\Sigma_I(R)$ between the data and the fit are displayed in the bottom panel. The large residuals at $R < 0.66$ arcsec are not significant.

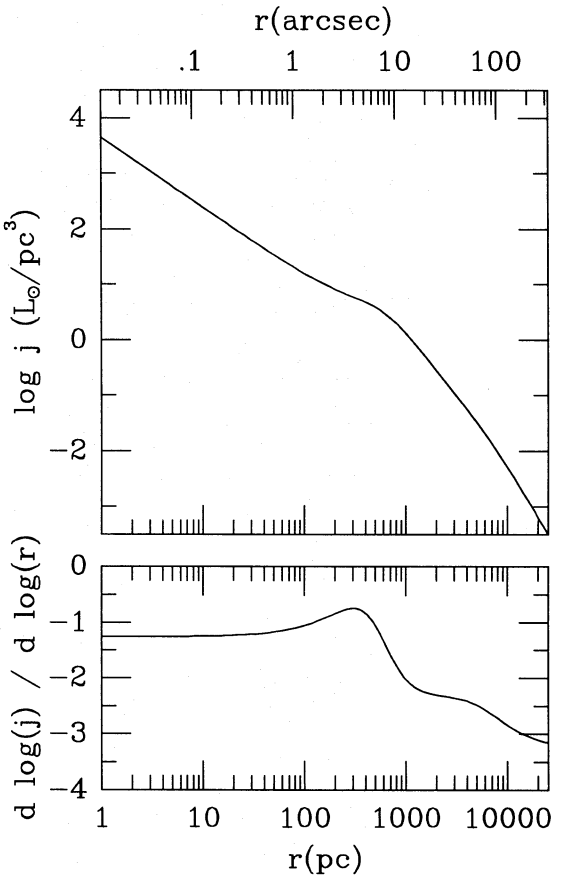

Figure 8. The top panel shows the *I*-band luminosity density profile of M87, obtained by deprojecting the intensity profile in equation (6). At small radii, $j \propto r^{-1.26}$. A distance of 16 Mpc was assumed, i.e. 1 arcsec = 77.6 pc. The scale on the abscissa is in pc; the corresponding scale in arcsec is shown at the top. The bottom panel shows the logarithmic slope of $j(r)$.

$A_B = 0.09$ quoted by the RC3 (de Vaucouleurs et al. 1991) and the ratio $A_B/A_I \approx 2.1$ suggested by the data of Johnson (1965).

To avoid noise amplification in the modelling, we have used a smooth fit to the observed projected intensities, of the form

$$I(R) = I_0 (R/a_1)^{-s_0} [1 + (R/a_1)^{\alpha_1}]^{-s_1/\alpha_1} [1 + (R/a_2)\,\alpha_2]^{-s_2/\alpha_2}. \quad (6)$$

The quantities s_0 and $I_0 a_1^{s_0}$ were fixed so as to the the slope and amplitude of the central cusp observed with the *HST*. The remaining parameters were determined by least-squares fitting to the data. The best fit has $a_1 = 7.47$ arcsec, $a_2 = 90.17$ arcsec; $s_0 = 0.26$, $s_1 = 1.09$, $s_2 = 0.88$, $\alpha_1 = 3.31$, $\alpha_2 = 2.11$ and $I_0 = 7.7033 \times 10^9\ \mathrm{L}_{\odot,I}\ \mathrm{kpc}^{-2}$. The quantity I_0 corresponds to an *I*-band surface brightness of 15.875 mag arcsec^{-2}, independent of the distance of M87. The functional form of equation (6) has no physical significance, but was adopted merely because it fits the data well. The surface brightness profile of the model is compared to the data in Fig. 7. The rms residual for $R \geq 0.66$ arcsec is only 0.01 mag arcsec^{-2}, of the same order as the formal errors in the data. The larger residuals for $R < 0.66$ arcsec are not significant. Lauer et al. (1992) showed that an $I(R) \propto R^{-0.26}$ power-law cusp for $R < 0.66$ arcsec (as in our model) fits the *HST* data well.

We construct spherical models for M87. The observed ellipticity of M87 is $\varepsilon \lesssim 0.07$ for 1 arcsec $\lesssim R \lesssim 15$ arcsec (Lauer et al. 1992). It rises slowly to $\varepsilon \approx 0.15$ at 163 arcsec (Peletier et al. 1990). The observed ellipticity is small enough to justify our approach (although it is also possible that M87 is a flattened system seen nearly face-on). For a spherical system, the luminosity density $j(r)$ is related to the projected intensity $I(R)$ through the Abel transform:

$$j(r) = -\frac{1}{\pi} \int_r^\infty \left[\frac{\mathrm{d}I}{\mathrm{d}R}\right](R) \frac{\mathrm{d}R}{\sqrt{R^2 - r^2}} \quad (7)$$

(e.g. Binney & Tremaine 1987). We assume a distance $D = 16$ Mpc for M87. At this radius, 1 arcsec = 77.6 pc. The luminosity density $j(r)$ corresponding to the projected intensity $I(R)$ in equation (6) is easily calculated numerically, and is displayed in Fig. 8. The quantity d log j/d log r is also shown.

Near the centre, the luminosity density has a central $j \propto r^{-1.26}$ cusp. Interestingly, $j(r)$ has an inflexion point at $r = 3.90$ arcsec. At this radius, d log j/d log $r = -0.744$. The M87 luminosity density does not therefore turn over smoothly from a steep power law in the outer parts to a shallower power law in the inner parts, as does the projected

surface brightness in equation (6). It turns over into a shallow power law at $r \approx 10$ arcsec, but steepens again in the central few arcsec. Interestingly, similar profiles are observed in models of the adiabatic growth of a central black hole into a galaxy model with a pre-existing core (Young et al. 1978; Young 1980).

To test whether the inflexion point in $j(r)$ could be an artefact due to the particular form of our parametrization in equation (6), we also attempted the opposite approach: fitting the projected intensities of parametrized luminosity densities to the observations. This approach always yielded the same inflexion point, as seen in Fig. 8. When a parametrization for $j(r)$ that could not develop an inflexion point was chosen, the resulting fit to the data was always much worse (rms residual $\gtrsim 0.05$ mag arcsec^{-2}) than the fit in Fig. 7. The inflexion point in $j(r)$ thus appears to be a real feature of the M87 luminosity density profile. However, a more sophisticated unparametrized analysis (along the lines discussed by Merritt & Tremblay 1994) is required to demonstrate its presence beyond doubt.

6.2 Hydrostatic equilibrium models

The mass density of the stars is given by $\rho(r) = (M/L)j(r)$, where (M/L) is the (unknown) mass-to-light ratio of the stars. Henceforth we use the quantity $\Upsilon \equiv (M/L)/(M/L)_\odot$. It is assumed that Υ is independent of radius. The potential of the stars is

$$\Phi_*(r) = -4\pi G\left[\frac{1}{r}\int_0^r \rho(r')r'^2\,\mathrm{d}r' + \int_r^\infty \rho(r')r'\,\mathrm{d}r'\right]. \tag{8}$$

The total potential Φ is the sum of Φ_* and a (possible) contribution $GM_{\rm BH}/r$ from a central black hole with (unknown) mass $M_{\rm BH}$.

The Jeans equation for hydrostatic equilibrium in a spherical stellar system is

$$\frac{\mathrm{d}(\rho\sigma_r^2)}{\mathrm{d}r} + 2\frac{\beta\rho\sigma_r^2}{r} = -\rho\frac{\mathrm{d}\Phi}{\mathrm{d}r}, \tag{9}$$

where the function $\beta(r) \equiv 1 - (\sigma_\theta^2/\sigma_r^2)$ measures the (unknown) velocity dispersion anisotropy of the stars. Models with $\beta = 0$ are isotropic, models with $\beta < 0$ are tangentially anisotropic and models with $0 < \beta \leq 1$ are radially anisotropic. We construct models without mean streaming, and hence $\sigma_\phi^2 = \sigma_\theta^2$.

Binney & Mamon (1982) described an algorithm to calculate, for any given black hole mass (including zero), the unique mass-to-light ratio Υ and anisotropy function $\beta(r)$ that produce a given projected line-of-sight velocity dispersion profile $\sigma_{\rm p}(R)$. They used their algorithm to recover the function $\beta(r)$ that was consistent with the then available kinematical data for M87, assuming there is no central black hole. A disadvantage of their elegant method is that it requires knowledge of the projected velocity dispersions, *corrected for the effects of seeing and spatial binning*. Such corrections can be exceedingly difficult to make, especially near the centre. In the present paper, we therefore use the opposite approach. We calculate the expected velocity dispersions for a given function β(r), taking the setup and seeing of the observations into account, and compare the results to the data.

Equation (9) is a linear, first-order differential equation for $\rho\sigma_r^2$, with solution

$$\rho\sigma_r^2(r) = \int_r^\infty \rho(r')\left(\frac{\mathrm{d}\Phi}{\mathrm{d}r}\right)(r')\exp\left[2\int_r^{r'}\frac{\beta(r'')\,\mathrm{d}r''}{r''}\right]\mathrm{d}r'. \tag{10}$$

This is a special case of a more general solution for certain classes of axisymmetric systems (Bacon, Simien & Monnet 1983). We consider anisotropy functions of the form

$$\beta(r) = (\beta_\infty r^2 + \beta_0 r_a^2)/(r^2 + r_a^2) \tag{11}$$

(Qian 1993), where $r_a > 0$ is a characteristic anisotropy radius, $\beta_0 \leq 1$ is the central value of β, and $\beta_\infty \leq 1$ is the asymptotic value at large radii. If $\beta_0 = \beta_\infty$, then $\beta(r)$ is constant. With equation (11), the expression for $\sigma_r^2(r)$ reduces to

$$\rho\sigma_r^2(r) = \int_r^\infty \rho(r')\left(\frac{\mathrm{d}\Phi}{\mathrm{d}r}\right)(r')\left(\frac{r'^2 + r_a^2}{r^2 + r_a^2}\right)^{\beta_\infty} \times\left[\left(\frac{r'^2}{r^2}\right)\Big/\left(\frac{r'^2 + r_a^2}{r^2 + r_a^2}\right)\right]^{\beta_0}\mathrm{d}r', \tag{12}$$

which is always positive. Equation (12) allows σ_r^2 to be evaluated numerically for any combination of Υ, $M_{\rm BH}$, β_0, β_∞ and r_a. Predictions for the observed velocity dispersion at each radius along the slit are then obtained as follows (in analogy to the discussion in section 3.3 of Paper II). In a position at galactocentric distance r that projects to a galactocentric distance R, the line-of-sight velocity dispersion $\sigma_{\rm l}$ satisfies $\sigma_{\rm l}^2 = \sigma_r^2\{1 - [\beta(r)R^2/r^2]\}$. Upon projection of $\rho\sigma_{\rm l}^2$, one obtains the product $I\sigma_{\rm p}^2$ of the intensity and the squared projected velocity dispersion. The predicted velocity dispersions are then obtained by convolving both $I\sigma_{\rm p}^2$ and I with the PSF of our observations, binning both into pixels as appropriate for our observational setup, and taking the ratio of both quantities.

6.3 Asymptotic behaviour at small radii

For $r \to 0$, one has $\beta \approx \beta_0$ and $\rho(r) \propto r^{-\delta}$ ($\delta \equiv 1.26$). The mass $M(r)$ inside radius r is $M(r) \propto r^{3-\delta}$, if there is no central black hole, and $M(r) \approx M_{\rm BH}$ if there is a central black hole. With these expressions, the Jeans equation (9) can be solved to obtain the asymptotic behaviour of σ_r^2 at small radii. If there is no central black hole, the solutions are of the form

$$\sigma_r^2 = c_1 r^{\delta - 2\beta_0} + c_2 r^{2-\delta}, \qquad (M_{\rm BH} = 0,\ r \to 0), \tag{13}$$

where c_1 and c_2 are constants (fixed by the boundary conditions). The asymptotic behaviour at small radii is

$$\sigma_r^2 \propto \begin{cases} r^{\delta - 2\beta_0}, & (\beta_0 \geq \delta - 1), \\ r^{2-\delta}, & (\beta_0 \leq \delta - 1). \end{cases} \tag{14}$$

The velocity dispersion diverges for $r \to 0$ if $\beta_0 > \delta/2 = 0.63$, it converges to a constant for $\beta_0 = \delta/2$, and it converges to zero for $\beta_0 < \delta/2$. The projected velocity dispersions also diverge for $\beta_0 > \delta/2$. For $\beta_0 = 0$, our results agree with those of Dehnen (1993) and Tremaine et al. (1994), who discuss a

set of isotropic dynamical models with the cusp steepness δ as a free parameter. If there is a central black hole, the solutions are of the form

$$\sigma_r^2 = c_1 r^{\delta-2\beta_0} + c_2 r^{-1} \qquad (M_{\rm BH} \neq 0, r \to 0). \tag{15}$$

The asymptotic behaviour at small radii is then $\sigma_r^2 \propto r^{-1}$ for all $\beta_0 \leq 1$.

As an illustration of equation (14), we show in Fig. 9 the predicted σ_r for models with constant $\beta(r)$, fixed Υ_I (taken to be 2.941 for the purpose of this figure) and no black hole. At large radii, $\sigma_r \propto r^{-1/2}$, since our model for M87 has finite mass. Fig. 10 shows the projected (but not seeing-convolved) velocity dispersions for these models. In models with large radial motion, the projected velocity dispersion is large in the inner parts and small in the outer parts. For models with large tangential motion, it is the other way around.

6.4 Fitting the data

We first consider models for M87 without a central black hole. We start with the simplest models, those with constant β. To compare the predicted $\sigma(R)$ of our models with the observed velocity dispersions σ_i at radii R_i $(i=1,\ldots N)$, we define

$$\chi_\sigma^2 \equiv \sum_{i=1}^{N} \left[\frac{\sigma_i - \sigma(R_i)}{\Delta\sigma_i} \right]^2. \tag{16}$$

For fixed constant β and $M_{\rm BH}=0$, the mass-to-light ratio Υ is the only free parameter of the model. For each β we can choose it so as to minimize χ_σ^2. Fig. 11 displays the resulting fits to the data for several values of β. In contrast to Fig. 10, each of the models now has a different Υ, and seeing and spatial binning have been taken into account. This makes a large difference, especially near the centre. The value of β that produces the lowest overall χ_σ^2 is $\beta=0.478$. The corresponding best-fitting I-band mass-to-light ratio is $\Upsilon_I=2.941$. The curve labelled 'A' in Fig. 12 shows the fit of this model to the data. The quantity $\chi_\sigma^2=52.15$ for 41 degrees of freedom. The probability of a value of χ_σ^2 this large (or larger) occurring by chance is 11 per cent. Hence the fit of this model to the data is statistically acceptable. The formal error on β (i.e. the variation in β required to increase χ_σ^2 by one with respect to its minimum value) is very small: $\Delta\beta=0.013$. The formal error on Υ_I is 0.032.

We argued in Section 5.5 that the observed central dip in the velocity dispersion might not be real. If so, the projected, seeing-convolved velocity dispersion could be ~ 400 km s^{-1} everywhere inside the central arcsec. The predictions of the $\beta=0.478$ model are then too low near the centre. Equation (10) demonstrates that the predicted dispersions near the centre can be increased by increasing β near the centre. As an example, the curve labelled 'B' in Fig. 12 shows the predictions of a model with $\beta_0=0.65$, $\beta_\infty=0.478$, $r_a=2.5$ arcsec and $\Upsilon_I=2.887$.

Our models confirm the conclusion of Binney & Mamon (1982) and other authors, that the observed velocity dispersions for M87 do not necessarily imply the presence of a

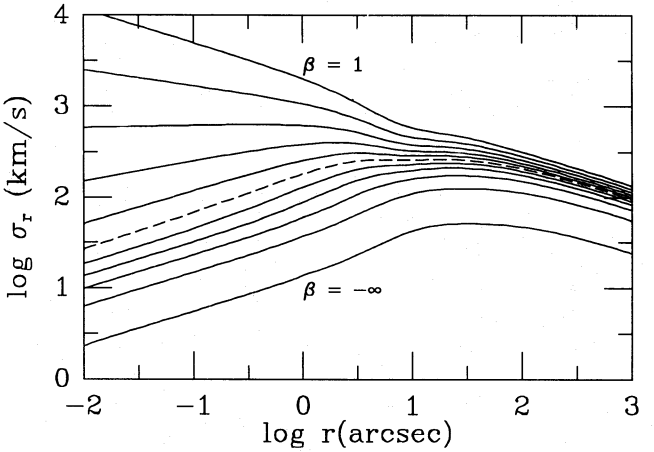

Figure 9. Predictions for the radial velocity dispersion σ_r, for models with constant β. The curves correspond to, from top to bottom, $\beta=1$, 0.8, 0.6, 0.4, 0.2, 0.0 (=isotropic=dashed curve), -0.25, -0.667, -1.5, -4 and $-\infty$. These models have mass-to-light ratio $\Upsilon_I=2.941$, and no central black hole.

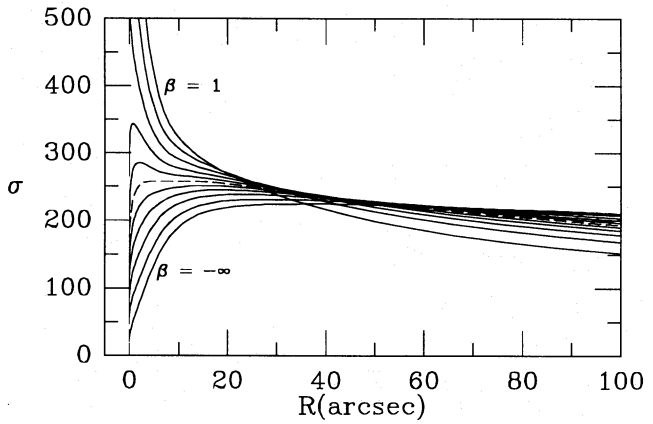

Figure 10. The projected (but not seeing-convolved) line-of-sight velocity dispersions for the models in Fig. 9.

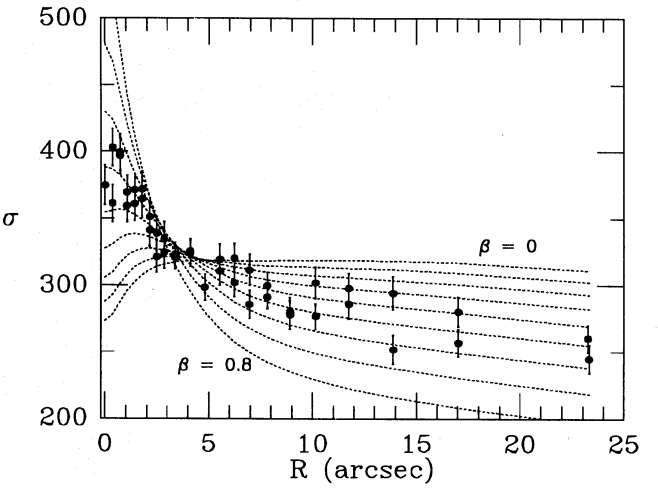

Figure 11. The data points show the velocity dispersions derived from the blue G-band data. Data points at negative radii were flipped to positive radii. The dotted curves show the (seeing-convolved and binned) predictions of models with constant β, from $\beta=0$ to 0.8 in steps of 0.1. These models have no central black hole. For each β, the mass-to-light ratio was chosen so as to minimize the quantity χ_σ^2, defined in the text. The predictions for the value of β that provides the best fit, $\beta=0.478$, are shown in Fig. 12 (curve 'A').

central black hole. The model of Binney & Mamon has $\beta \approx 0.2$ at $R = 0.5$ arcsec, $\beta \approx 0.9$ at $R = 1.5$ arcsec and $\beta \approx 0.4$ for 2 arcsec $\lesssim R \lesssim 15$ arcsec. The latter value is not dissimilar to the value $\beta = 0.478$ implied by our models. At smaller radii, however, our models differ from that of Binney & Mamon: our models do not require values of β as high as 0.9, nor do they require drastic variations in β near the centre. We attribute these differences to the poor spatial resolution of the data used by Binney & Mamon, which they do not explicitly take into account in their models. The Sargent et al. (1978) data were taken with 5.4-arcsec pixels, 15 times wider than our pixels. In addition, Binney & Mamon link these data to the single data point of Dressler (1980), which was obtained with very different spatial resolution. Binney & Mamon (1982) infer a V-band mass-to-light ratio $\Upsilon_V = 7.61$, corresponding to $\Upsilon_I = 3.58$.

To reproduce the observed velocity dispersions with a model that has an isotropic velocity dispersion near the centre requires the presence of a central black hole. As an example, we have studied models with $\beta_0 = 0$, $\beta_\infty = 0.478$ and $r_a = 5$ arcsec. For each fixed choice for $M_{\rm BH}$, the mass-to-light ratio Υ is the only free parameter. As before, we choose Υ so as to minimize χ^2_σ. The black hole mass for which this yields the lowest overall χ^2_σ is $M_{\rm BH} = 3.06 \times 10^9\ {\rm M}_\odot$, with corresponding mass-to-light ratio $\Upsilon = 2.738$. This model is labelled 'C' in Fig. 12. The dotted curve in Fig. 12 shows the predictions for the same model, but without the central black hole. Model C also provides a reasonably acceptable fit to the data. Our new measurements of the velocity dispersion in M87 therefore provide no strong evidence either for or against the presence of a massive central black hole.

Fully isotropic models for M87 [$\beta(r) \equiv 0$] predict the observed velocity dispersion to be approximately constant for 5 arcsec $\lesssim R \lesssim 25$ arcsec; cf. Fig. 10. Hence such models cannot reproduce the gradually falling velocity dispersion profile that is observed (which requires $\beta \approx 0.478$). None the less, we display in Fig. 13 the predictions of isotropic models for M87, with $\Upsilon_I = 3.9$ and different black hole masses. Although none of the models provides a particularly good fit to the data, these models do imply a similar black hole mass as inferred above.

Winsall & Freeman (1993) report a velocity dispersion $\sigma = 238 \pm 12$ km s^{-1} at $R = 101.9$ arcsec (comparable to the effective radius of M87), from deep observations at very low surface brightness. Our models with $\beta_\infty = 0.478$ (A, B and C in Fig. 12) predict $\sigma \approx 182$ km s^{-1} at this radius. Our isotropic models (Fig. 13) predict $\sigma \approx 221$ km s^{-1}. To model data at such large radii properly, however, one should explicitly take the influence of the dark halo of M87 into account (Fabricant & Gorenstein 1983; Mould et al. 1990; Merritt & Tremblay 1993).

6.5 Aperture dispersions

With the *HST* it might soon be possible to study the M87 stellar kinematics with much higher spatial resolution than has been possible from Earth. It is therefore interesting to consider also the predictions of our models at higher spatial resolution. To this end we have calculated 'aperture dispersions' for our models, i.e. the velocity dispersion expected for observations through a circular aperture centred on the galaxy (see also Tremaine et al. 1994). Fig. 14 displays the aperture dispersions $\sigma_{\rm A}$ for the models displayed in Fig. 12, as a function of the aperture diameter D. At Earth-based spatial resolution ($D \gtrsim 1$ arcsec) the models A, B and C predict a similar velocity dispersion. At higher resolution, model C with a central black hole predicts a much larger velocity dispersion than the anisotropic models without a black hole. In van der Marel (1994), however, we demonstrate that, for observations at *HST* resolution, models with a black hole have a central VP that deviates significantly from a Gaussian. The VP wings are much more extended than those of a Gaussian, and, as a result, traditional techniques for the analysis of galaxy spectra will seriously underestimate the true velocity dispersion (see also Section 7 below). Modelling of VP shapes, in addition to velocity dispersions, is thus essential for the proper interpretation of *HST* spectra.

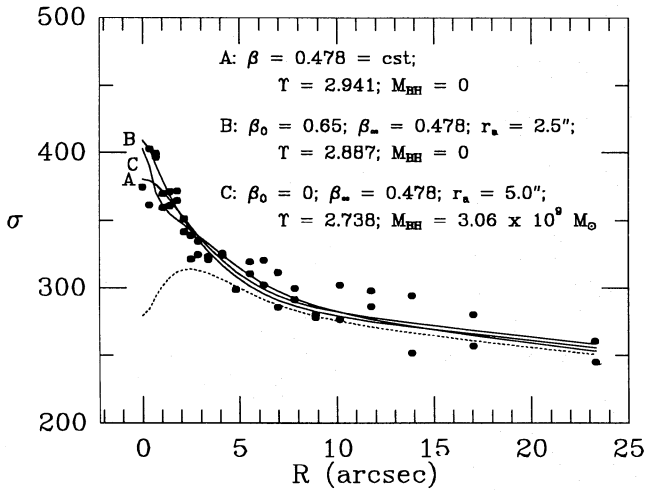

Figure 12. Predicted (seeing-convolved and binned) velocity dispersions of different models for M87. Models A and B are radially anisotropic and have no central black hole. Model A has constant β whereas model B has a larger value of β in the centre than in the outer parts. Model C is isotropic near the centre and has a central black hole. The dotted curve shows the predictions of model C when the black hole is removed. The data points are as in Fig. 11, but the error bars are omitted. All three models provide a reasonable fit to the data.

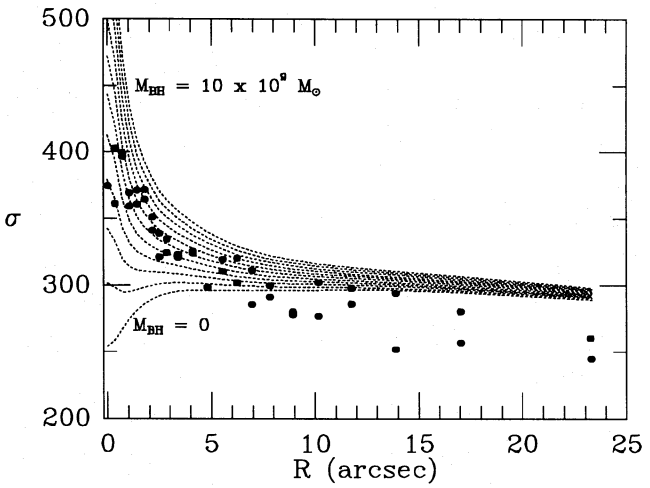

Figure 13. Predicted (seeing-convolved and binned) velocity dispersions for isotropic models of M87. All models have mass-to-light ratio $\Upsilon_I = 3.9$. The black hole masses are $M_{\rm BH} = 0$, 1, 2,... $10 \times 10^9\ {\rm M}_\odot$, respectively.

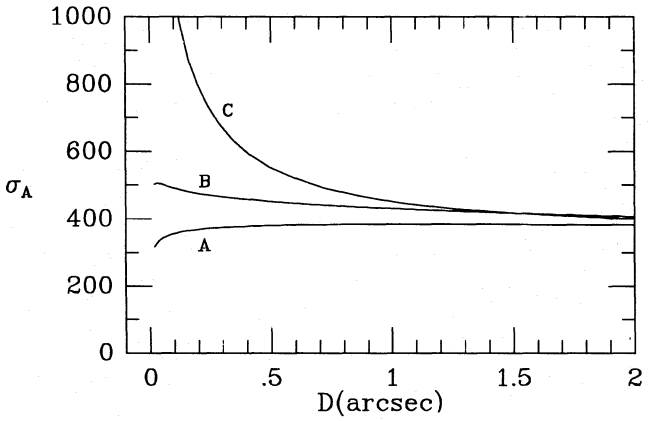

Figure 14. Shown is the 'aperture dispersion' σ_A for the three models in Fig. 12, as a function of the aperture diameter D.

7 VELOCITY PROFILES OF ISOTROPIC MODELS WITH A BLACK HOLE

In this section, we study the effect of a black hole on the observed VPs, especially near the centre. We restrict ourselves to isotropic models, for which the full distribution function of the stars can be recovered for any given mass density and potential (see below). Fig. 13 shows that isotropic models cannot provide a very good fit to the observed velocity dispersions for M87 outside the central 5 arcsec. The models in this section are therefore intended mainly to illustrate the general properties of models with a central black hole. Several of our results are evident also in the work of Bahcall & Wolf (1976), who calculated VPs of isotropic models with a central black hole and $\rho(r) \propto r^{-7/4}$ at small radii.

7.1 Calculation of velocity profiles

The distribution function (DF) for an isotropic spherical model is given by Eddington's formula:

$$f(\mathscr{E}) = \frac{1}{\pi^2\sqrt{8}} \frac{\mathrm{d}}{\mathrm{d}\mathscr{E}} \int_0^{\mathscr{E}} \left(\frac{\mathrm{d}\rho}{\mathrm{d}\Psi}\right)_{\Psi'} \frac{\mathrm{d}\Psi'}{\sqrt{\mathscr{E}-\Psi'}}, \tag{17}$$

where $\mathscr{E} \equiv \Psi(r) - (1/2)v^2$ is the relative energy of a star and $\Psi \equiv -\Phi$ is the relative potential (Binney & Tremaine 1987). We adopt a Cartesian coordinate system, with the z-axis along the line of sight and the x- and y-axes in the plane of the sky. At any particular point in the galaxy, the local (i.e. unprojected) distribution of stars over line-of-sight velocities is

$$\begin{aligned}\mathscr{L}_{\mathrm{loc}}(v_z; r) &\equiv \frac{1}{\rho(r)} \iint f(\mathscr{E})\, \mathrm{d}v_x\, \mathrm{d}v_y \\ &= \frac{1}{\rho(r)\pi\sqrt{2}} \int_0^{\Psi(r)-(1/2)v_z^2} \\ &\times \left(\frac{\mathrm{d}\rho}{\mathrm{d}\Psi}\right)_{\Psi'} \frac{\mathrm{d}\Psi'}{\sqrt{\Psi(r)-(1/2)v_z^2-\Psi'}}.\end{aligned} \tag{18}$$

The equality is obtained by defining polar coordinates in the (v_x, v_y) plane, changing the integration variable to $\mathscr{E}$ and substituting for $f(\mathscr{E})$ from equation (17). The upper bound of the integration follows from the fact that, for a system of finite mass, $f(\mathscr{E}) = 0$ for $\mathscr{E} \leq 0$. For any fixed mass-to-light ratio Υ and black hole mass M_{BH}, equation (18) can be evaluated numerically using the mass density and potential calculated in Section 6.

The normalized VP at a projected galactocentric distance R from the centre is

$$\mathscr{L}(v_z; R) \equiv \int_R^{r_{\max}(v_z)} \frac{2r\rho(r)\mathscr{L}_{\mathrm{loc}}(v_z; r)\,\mathrm{d}r}{\sqrt{r^2-R^2}} \Bigg/ \left[\int_R^{\infty} \frac{2r\rho(r)\,\mathrm{d}r}{\sqrt{r^2-R^2}}\right], \tag{19}$$

where $r_{\max}(v_z)$ satisfies $\Psi(r_{\max}) \equiv (1/2)v_z^2$. We model the seeing convolution, slit width and spatial binning of our observations, by integrating over the plane of the sky with the appropriate weighting function. In our isotropic non-rotating models, the VPs are always symmetric: $\mathscr{L}(v_z) = \mathscr{L}(-v_z)$.

7.2 Derived quantities

It is useful to analyse model VPs by calculating a number of characteristic quantities. First, we calculate for each VP the true rms velocity. This is the quantity that was discussed in Section 6 and is plotted in, for example, Fig. 13. Secondly, we calculate the parameters γ and σ of the best-fitting Gaussian, as well as the Gauss–Hermite moments h_4 and h_6, defined by equation (3). Thirdly, we convolve each model VP with our blue template spectrum and analyse the result with the method in Appendix A, to simulate the analysis of real data. The mean of the VP and the Gauss–Hermite moments of odd order are always zero for symmetric VPs, and are thus not discussed. In our models, we assume the true line strength to be 1; i.e. we do not address here the influence of the central luminosity spike of M87.

The various quantities described above can differ significantly. The values of γ and σ obtained by fitting a Gaussian to the VP differ from the true line strength and velocity dispersion if the true VP is not Gaussian (see also vdMF). In addition, the values of γ, σ, h_4 and h_6 obtained from the analysis of a spectrum generally differ from the values obtained by fitting to the VP directly. This is due to the fact that, in the analysis of real spectra, low-frequency information is lost due to continuum subtraction.

7.3 Applications

We calculated the VPs expected for the central pixel of our blue G-band setup, assuming a black hole mass of 0, 1, 2,... $10 \times 10^9\ \mathrm{M}_\odot$, respectively. The mass-to-light ratio was taken to be $\Upsilon_I = 3.9$, as in Fig. 13. It was verified that the DF (equation 17) is positive definite for each of these values. The VPs for some representative values of M_{BH} are displayed in Fig. 15. The quantities that characterize the VP shape (as discussed in Section 7.2) are displayed in Fig. 16.

The model without a central black hole is not relevant for M87, since its velocity dispersion profile as a function of radius is markedly different from the observed profile; cf.

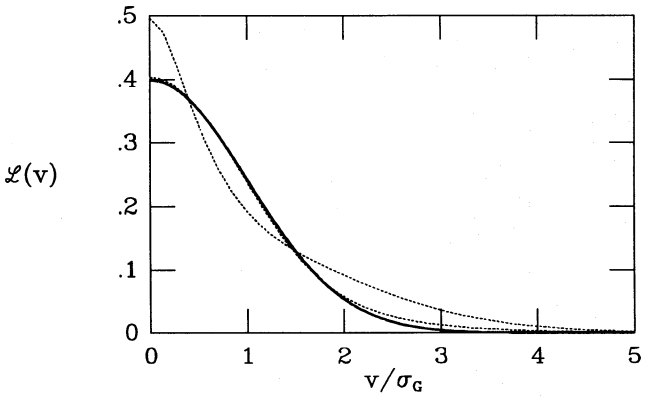

Figure 15. Predicted (seeing-convolved and binned) VP shapes for the centre of M87, for the observational setup of our blue G-band observations. The thick solid curve is the standard Gaussian (i.e. normalized and with dispersion one). The VPs are for isotropic models with $\Upsilon_I = 3.9$ and black hole masses of 0 (this is the VP that deviates most noticeably from the standard Gaussian), 2×10^9 $M_\odot$ (this VP entirely overlays the standard Gaussian) and 10×10^9 $M_\odot$ (this is the VP that has slightly broader wings than the standard Gaussian). The horizontal and vertical scales for each VP were chosen to make the best-fitting Gaussian coincide with the standard Gaussian. The quantity σ_G in the label of the abscissa denotes the dispersion of the best-fitting Gaussian.

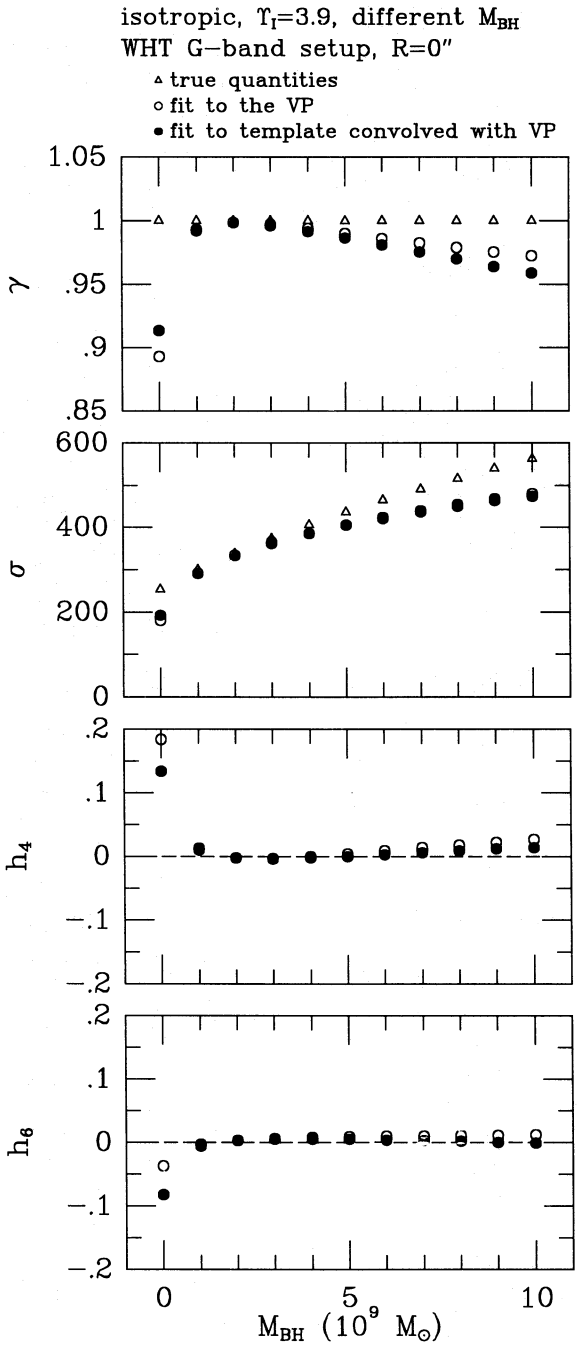

Figure 16. Predicted (seeing-convolved and binned) quantities for the centre of M87, for the observational setup of our blue G-band observations. The models are isotropic with $\Upsilon_I = 3.9$ and have different black hole masses (set out on the abscissa). The displayed quantities are discussed in Section 7.2. Open triangles denote the true line strength ($\equiv 1$) and rms velocity; open circles are quantities obtained by fitting a Gaussian to the VP and determining the Gauss–Hermite moments, as in equation (3); solid circles are quantities obtained by analysing the convolution of the VP and our blue template spectrum, using the method in Appendix A.

Fig. 13. The central VP is very different from a Gaussian, as witnessed by the strongly non-zero values of h_4 and h_6. This is due to the large variation in the velocity dispersion along the line of sight (which is zero in the centre but rises steeply to a value of a few hundred km s^{-1}; cf. Fig. 9). Merely fitting a Gaussian to the convolved spectrum yields strongly biased estimates for the line strength and velocity dispersion. The model with a 2×10^9 $M_\odot$ black hole has a central VP that is very close to Gaussian; cf. Fig. 15. The Gauss–Hermite moments h_4 and h_6 are approximately zero, and the estimates for γ and σ, obtained by fitting a Gaussian to the convolved spectrum, are good estimates of the true line strength and velocity dispersion. For larger black hole masses, the velocity dispersion increases. In addition, the wings of the VP become more extended than those of a Gaussian, as illustrated by the $M_{BH} = 10 \times 10^9$ $M_\odot$ model in Fig. 15. This is due to the stars that orbit close to the hole at high velocities. In van der Marel (1994), it is demonstrated that the wings fall off asymptotically as a power law, $\mathscr{L}(v_z) \propto |v_z|^{-7+2\delta}$, with $\delta = 1.26$ for M87. The wings contribute significantly to the normalization and the dispersion of the velocity profile. A Gaussian fit to the velocity profile is insensitive to the wings, and thus underestimates both the line strength γ and the velocity dispersion σ. In the analysis of real data, this effect is even more pronounced, because information on the wings is lost due to continuum subtraction. Fig. 16 shows that the expected errors in γ and σ are substantial, in spite of the fact that, to the eye, the VP appears to be very close to a Gaussian. At *HST* resolution, these errors are much larger still (van der Marel 1994). The expected signature in the Gauss–Hermite moments h_4 and h_6 is only very small (cf. Fig. 16), due to the fact that these are [by their definition, see equation (3)] not very sensitive to the wings of the VP. (In fact, this is why they can be reasonably robustly measured from real data.)

The isotropic model that seems most appropriate for M87 is the one with $M_{BH} = 5 \times 10^9$ $M_\odot$. Fig. 17 shows the predicted quantities for this model as a function of position

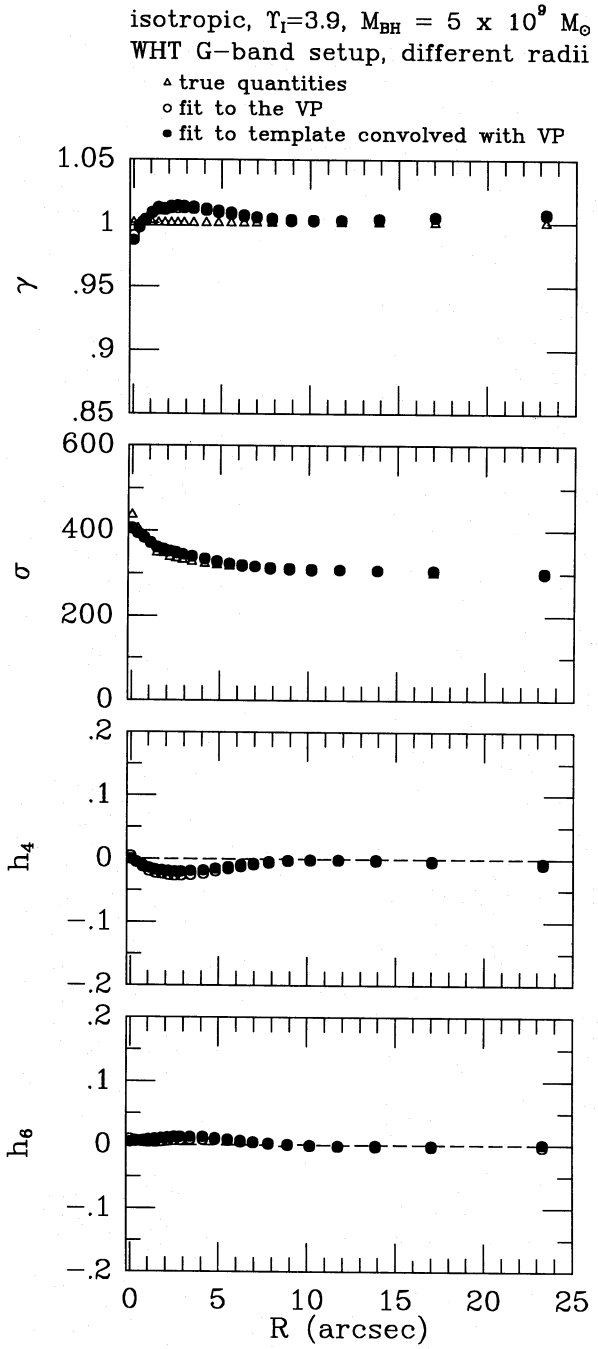

Figure 17. Predicted (seeing-convolved and binned) quantities of isotropic models for M87, with $\Upsilon_I = 3.9$ and $M_{BH} = 5 \times 10^9$ $M_\odot$, for the observational setup of our blue G-band observations. The abscissa is the radius along the slit. The symbols are as in Fig. 16.

along the slit. The small values of h_4 and h_6 are not inconsistent with our observations (see Fig. 4a). The velocity dispersion that one would expect to observe (solid dots in Fig. 17) falls from ~400 km s^{-1} in the centre to ~330 km s^{-1} at $R = 5$ arcsec, similar to what is observed. The true central velocity dispersion is underestimated by ~35 km s^{-1} (i.e. ~8 per cent), but this is not so much that the 'inferred' velocity dispersion has a central minimum (which is what is observed; cf. Fig. 4a). Fig. 17 demonstrates that the central line strength will be underestimated by ~2 per cent. The line strengths outside the very centre will be slightly overestimated, and one would thus expect to observe a central dip in the line strength of ~4 per cent. This might explain the result of Section 5.4, that the central line strength of M87 inferred from the blue data is too small to be consistent with the *HST* photometry (cf. Fig. 5). Although our models do not describe the observations in detail, they do suggest the presence of a central black hole as a qualitative explanation for the fact that both the central line strength and the central velocity dispersion derived from our blue data appear to be underestimated.

Dressler & Richstone (1990) set an upper limit of 4×10^9 $M_\odot$ on the mass of a possible black hole in M87. They compared the velocity dispersions determined from fitting a Gaussian VP to the data to the true velocity dispersions of their models. The above results demonstrate that the interpretation of the observed velocity dispersions near the centre is more complicated than was previously thought, if a central black hole is indeed present. The effects that we have discussed are in the sense that previous studies might have *under*estimated the mass of a possible central black hole. Hence the upper limit of Dressler & Richstone should probably be increased.

The systematic errors discussed above for M87 are not expected to be as severe for M32, which we studied in Paper II. Because of its lower velocity dispersion (~50 km s^{-1}), continuum subtraction is not so much of a problem. The VP wings of axisymmetric models for M32 with a central black hole are studied in detail by Qian et al. (1994).

8 DISTRIBUTION FUNCTIONS FOR ANISOTROPIC MODELS

In general, there exist infinitely many distribution functions $f(\mathscr{E}, L^2)$ that can generate a given mass density $\rho(r)$, potential $\Psi(r)$ and velocity dispersion anisotropy function $\beta(r)$. A useful approach in the construction of anisotropic models is to use an ansatz for the so-called 'augmented mass density' $\rho_a(r, \Psi)$, which does determine the distribution function $f(\mathscr{E}, L^2)$ uniquely (e.g. Dejonghe 1987). The augmented mass density is a mathematical tool without much physical significance. It must satisfy the obvious constraint that

$$\rho_a[r, \Psi(r)] = \rho(r). \tag{20}$$

In his PhD thesis, Qian (1993) discussed a method to obtain $f(\mathscr{E}, L^2)$ from $\rho_a(r, \Psi)$, through the use of a complex contour integral. The same method can also be applied to obtain the unique $f(\mathscr{E}, L_z^2)$ that generates a given axisymmetric mass density $\rho(R, z)$ (Hunter & Qian 1993). As an example, Qian considered a special class of models in which the augmented mass density is separable:

$$\rho_a[r, \Psi(r)] \equiv P(\Psi) D(r). \tag{21}$$

Models with the anisotropy function $\beta(r)$, as in equation (11), are obtained by setting

$$D(r) = r^{-2\beta_0}[1 + (r^2/r_a^2)]^{\beta_0 - \beta_\infty}. \tag{22}$$

With this choice for $D(r)$, the function $P(\Psi)$ is determined by equations (20) and (21). The contour integral method allows

$f(\mathscr{E}, L^2)$ to be recovered for any $\rho(r)$, $\Psi(r)$, β_0, β_∞ and r_a, although the distribution function is not guaranteed to be positive. Some special cases have been discussed before in the literature. For $\beta_0 = \beta_\infty$, the models have constant $\beta(r)$ and $f = g(\mathscr{E})L^{-2\beta_0}$ (e.g. Hénon 1973). For $\beta_0 = 0$ and $\beta_\infty = 1$, the distribution functions are of the form $f = f[\mathscr{E} - (L^2/2r_a^2)]$ (Osipkov 1979; Merritt 1985). For $\beta_\infty = 1$ and general β_0, the models have $f = g[\mathscr{E} - (L^2/2r_a^2)]L^{-2\beta_0}$ (Cuddeford 1991).

One can show that, in the limit $L^2 \to 0$, the contour integral for $f(\mathscr{E}, L^2)$ reduces to

$$\lim_{L^2\to 0} f(\mathscr{E}, L^2)L^{2\beta_0} = \frac{2^{\beta_0}}{\pi^{3/2}\sqrt{8}\,\Gamma(1-\beta_0)\Gamma(n+\beta_0-3/2)} \times \frac{\mathrm{d}^n}{\mathrm{d}\mathscr{E}^n}\int_0^{\mathscr{E}} \frac{P(\Psi)\,\mathrm{d}\Psi}{(\mathscr{E}-\Psi)^{-\beta_0-n+5/2}}, \qquad (23)$$

where n is any integer with $n > (3/2) - \beta_0$. For $\beta_0 = \beta_\infty$, i.e. $\beta(r) =$ constant, this expression is in fact valid for all L^2. For $\beta_0 = \beta_\infty = 0$, the expression can be reduced to equation (17).

We evaluated equation (23) for the three models, A, B and C, in Fig. 12. We found that, for each of the three models, there were values of $\mathscr{E}$ for which the result was negative. This implies that the distribution functions with separable augmented densities that reproduce the anisotropy functions $\beta(r)$ of these models are not positive definite, and are hence unphysical. This result can be understood intuitively by considering, as a simple example, the model with $\beta(r) = 1/2 =$ constant. Equation (23) then implies that the distribution function is

$$f(\mathscr{E}, L^2) \propto \frac{1}{L}\left(\frac{\mathrm{d}P}{\mathrm{d}\Psi}\right)_{\Psi=\mathscr{E}}. \qquad (24)$$

Since, for this model, $P(\Psi) = r\rho(r)$, the distribution function is positive definite if and only if

$$\frac{\mathrm{d}\log\rho}{\mathrm{d}\log r} < -1 \qquad (25)$$

for all r. Fig. 8 shows that this is not the case, although this does depend on whether the inflexion point in $j(r)$ is indeed real. We find that the range in energies for which the distribution function is negative is smallest for our model C [for which $\beta(r)$ is smallest at each radius] and largest for our model B [for which $\beta(r)$ is largest at each radius], as one would expect. The largest β for which the expression (23) is positive definite, for a model with $\beta(r) =$ constant, was found to be $\beta = 0.33$. This model, however, does not fit the observed velocity dispersions; cf. Fig. 11.

Our results show that it is much more difficult to construct a positive distribution function that fits the data, without invoking a central black hole, than it is to find a solution of the Jeans equation that does so. However, we have not shown that it is impossible to construct such a distribution function. After all, we have only considered a simple class of models: those with separable augmented density of the form of equation (21). Indeed several other authors (Newton & Binney 1984; Richstone & Tremaine 1985; Dejonghe 1989; Dressler & Richstone 1990) constructed radially anisotropic models for M87 that do have a positive distribution function. Thus, with more general techniques, it might in fact be possible to construct positive distribution functions for our models in Fig. 12. But even if it is, there is still the question of stability. Merritt (1987) used an N-body code to demonstrate that the Newton & Binney model is unstable to the formation of a bar near the centre, and hence cannot be a plausible model for M87. The Newton & Binney model fits the results of Binney & Mamon (1982) and hence has $\beta(r) \approx 0.85$ at $r = 1.5$ arcsec. It is not clear, a priori, to what extent Merritt's result hinges on the behaviour of the Binney & Mamon model near the centre. Our results in Section 6 demonstrate that $\beta(r)$ need not be as high near the centre as in the Binney & Mamon model, which might remove the instability. Palmer & Papaloizou (1987) argued that any model with $f \to \infty$ for $L^2 \to 0$ has unstable modes (although the growth rates might be very long). For the models discussed above, this is the case for $\beta_0 > 0$ (cf. equation 23). However, this is not necessarily true for all models with $\beta(r)$ as in equation (11). It might thus be possible to construct distribution functions for our models A and B, which have $\beta_0 > 0$, that are stable. Also, we could easily modify our models such that $\beta(r)$ drops rapidly to zero in, say, the central arcsec. This would decrease the predicted velocity dispersions near the centre slightly (see also Zeilinger, Møller & Stiavelli 1993), but this might even give a better fit to the data if the observed central dip in σ were real (contrary to our arguments in Section 5.5).

The existence and stability of anisotropic distribution functions for M87 are important issues to be readdressed in the near future. Once (and if) stable positive distribution functions have been found, they can be used to calculate VP shapes. By modelling the observed VPs, it might then be possible to constrain the velocity dispersion anisotropy of M87, and hence the mass of a possible central black hole (cf. Fig. 12).

9 IONIZED GAS KINEMATICS

Our observational study was not initiated specifically to study the kinematics of the ionized gas in M87. The Hγ emission line in our blue spectra is, however, strong enough to allow such a study. We use the residuals of the VP fits of Section 5. These residuals are the continuum- and starlight-subtracted galaxy spectra. A simple scheme was used to correct for the presence of the [O III] 4363.21-Å emission line in the redward wing of Hγ (see Fig. 3). We first fitted a Gaussian to the Hγ line at each radius, without bothering about the presence of the [O III] line. These results are used as models for the [O III] line, assuming a fixed flux ratio of 0.06 (cf. Section 4) and a velocity difference of $\Delta v = c\Delta \ln \lambda = 1566.6$ km s^{-1} at each radius. The models for the [O III] line are subtracted off to yield the 'deblended' data for the Hγ line. This subtraction of the [O III] line is admittedly crude. A more sophisticated scheme is not required though, given the low intensity of the [O III] line and the very large velocity difference with Hγ. We verified that all the results below are insensitive to the particular scheme adopted for subtracting the [O III] line.

The deblended data for the Hγ line are displayed in Fig. 18 (dotted curves). The intensity of the Hγ emission decreases rapidly with radius, but was found to be sufficient for kinematical analysis over the radial range -1.43 arcsec $\leq R \leq 2.86$ arcsec. The shape of the Hγ emission line

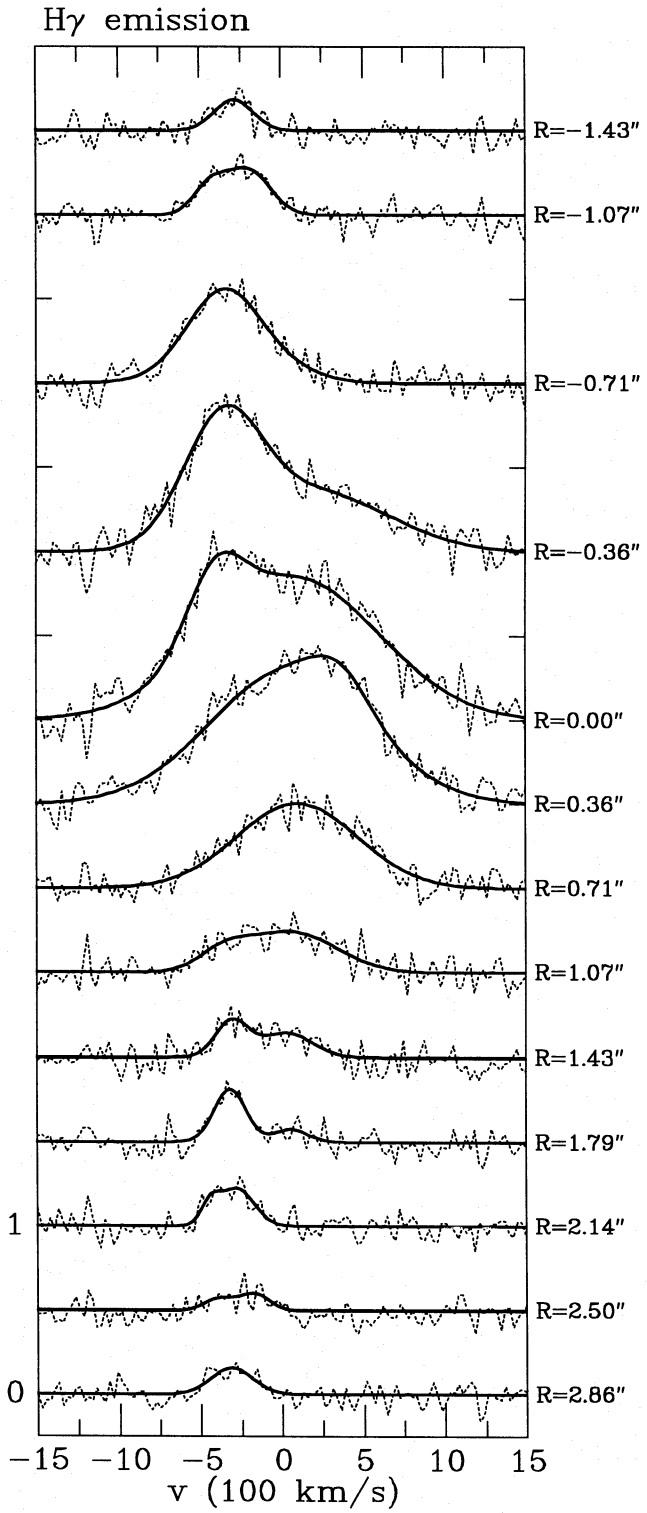

Figure 18. The dotted profiles show the Hγ emission-line spectrum as a function of position along the slit. The abscissa is in units of 100 km s^{-1}; $v=0$ corresponds to the systemic velocity. The underlying absorption-line spectrum and non-thermal continuum were subtracted, using the results of Section 5. The expected (small) contribution of the [O III] emission line at $v=1566.6$ km s^{-1} was subtracted as described in the text. Before plotting, each spectrum was divided by the amplitude of the Hγ line at $r=0$ arcsec. For each spectrum, zero is at the height of the label in the right margin and unity is two tick marks above that. The unequal spacing of the zero-points was chosen to avoid confusion and has no further significance. The solid curves are fits obtained as described in the text.

generally deviates from a Gaussian. The deviations are most significant in the central three pixels (i.e. $R=-0.36$, 0 and 0.36 arcsec), where they are presumably the result of the seeing convolution of an intrinsic velocity gradient. An alternative possibility, however, is that the gas consists of two (or more) physically distinct components. To characterize the emission-line shapes, we fitted the sum of the two Gaussians to the Hγ line at each radius. When this did not yield a significantly better fit (in a χ^2 sense) than the best-fitting single Gaussian, the latter was adopted. The fits are shown as solid curves in Fig. 18. They represent the data well. Fig. 19 shows the total flux, mean velocity and velocity dispersion at each radius, obtained by calculating the moments of the best fit to the data. The results are listed in Appendix B. These quantities are well defined observationally, even though their interpretation is not straightforward if the gas consists of more than a single component.

At positive radii, the flux of the Hγ emission falls off more gradually than at negative radii. The mean velocity of the gas at $R=0$ arcsec is 10.6 ± 11.4 km s^{-1}, consistent with the systemic velocity. The mean velocities at $R=-0.36$ and 0.36 arcsec are -78.6 ± 14.9 km s^{-1} and 74.1 ± 12.1 km s^{-1}, respectively, suggesting that the gas near the centre is in rotation. However, this is not true at large radii. For $r\gtrsim1$ arcsec, the mean velocity of the gas is negative at both negative and positive radii, indicating that this gas is not in

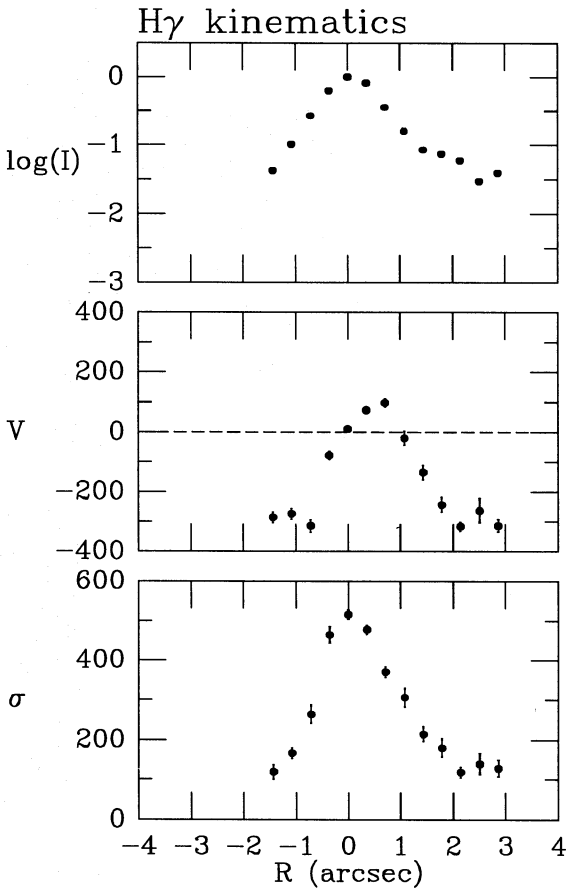

Figure 19. The logarithm of the total intensity, the mean velocity V and velocity dispersion σ of the Hγ emission line, as determined from the fits in Fig. 18. The quantities V and σ are in km s^{-1}. The intensity scale is arbitrary.

equilibrium. The velocity dispersion at $R=0$ arcsec is 516.2 ± 11.5 km s^{-1}, and falls off very steeply to ~ 125 km s^{-1} at $R \gtrsim 2$ arcsec.

The kinematics of the ionized gas in M87 have been studied previously by, for example, Sargent et al. (1978), Heckman et al. (1989), Jarvis (1990) and Sparks, Ford & Kinney (1993). These studies all indicated that the gas in and near the centre is blueshifted with respect to the systemic velocity. Fig. 19 indicates that, although the gas at $R \gtrsim 0.5$ arcsec is indeed blueshifted, the gas in the very centre is *not*. This was not detected by previous authors, because of the lower spatial resolution ($\gtrsim 2$ arcsec) of their data. Because of our higher spatial resolution, we also find a much higher central velocity dispersion than do previous authors. Sargent et al. (1978) and Heckman et al. (1989) found a central velocity dispersion of only ~ 300 km s^{-1}, a factor of 1.7 smaller than our value!

10 HYDROSTATIC EQUILIBRIUM MODELS FOR THE IONIZED GAS KINEMATICS

The distribution of the ionized gas in M87 has been studied by several authors using narrow-band imaging (e.g. Boksenberg et al. 1992; Sparks et al. 1993). In the inner ~ 4 arcsec, the isophotes of the ionized gas are roughly circularly symmetric, but at large radii the distribution of the ionized gas is filamentary. The gas might have originated from the accretion of a gas-rich dwarf. The mean velocities of the gas outside the very centre (Fig. 19; Sparks et al. 1993) indicate that it is not in hydrostatic equilibrium in the potential of the galaxy. This might also be true for the gas near the centre. Sparks et al. interpreted the blueshifts they observed near and in the centre as due to outflow, possibly the result of a small-scale galactic wind or due to the influence of the synchrotron jet.

Our observations show that the mean gas velocity in the very centre is consistent with the systemic velocity. This suggests an alternative explanation for the observed kinematics of the most tightly bound gas near the centre, namely bulk motion of individual gas clouds in the potential of M87. This was also suggested by Sargent et al. (1978), who used the formula $M(r) = rv_{\rm circ}^2/G$ to obtain an order of magnitude estimate for the total mass near the centre of M87. In view of the high spatial resolution of our data, we decided to study this possibility in some more detail. We therefore constructed some simple models, in which the gas is assumed to be in hydrostatic equilibrium. This is admittedly naive, as there remains the possibility of (contributions from) either infall or outflow, or of the presence of multiple components. Nevertheless, it does provide a useful estimate for the mass of a possible black hole in M87.

We assume the gas to be in a spherical configuration, consisting of individual clouds that orbit as test particles in the total potential of the stars and a possible central black hole. The gas itself is assumed not to contribute to the potential. We assume that the observed Hγ flux traces the surface mass density of the gas. This is not implied by the data, but is not inconsistent with it either. Both the geometry and the mass density of the gas are, in fact, poorly constrained by the data, because the observed Hγ intensity is related both to the mass density of the gas and to the (unknown) ionizing flux. The following model was adopted for the mass density of the gas:

$$\rho_{\rm gas} \propto [1 + (r/0.2 \text{ arcsec})^2]^{-1.8}. \quad (26)$$

Fig. 20 compares the observed Hγ flux with the predictions of the model, after projection on to the sky, convolution with the seeing and binning according to our observational setup. The fit is reasonable in the central 1.5 arcsec. We have not attempted to model the fact that the Hγ flux at negative radii is smaller than that at positive radii.

With the mass density of equation (26), we have calculated the velocity dispersion of the ionized gas using equation (10), assuming the velocity distribution of the gas clouds to be isotropic. The results are displayed in Fig. 20, for several assumed black hole masses. We assume $\Upsilon_I = 2.887$ for the stars, as for model B in Fig. 12. We compare the predictions in Fig. 20 both to the observed velocity dispersion of the gas and to the observed rms motion $\sqrt{V^2+\sigma^2}$. Given that our models cannot address the observed mean streaming, it is not quite clear to what quantity the predictions are best compared. Either way, both quantities only differ significantly outside the very centre, where our models are probably not correct anyway. In the absence of a black hole, the

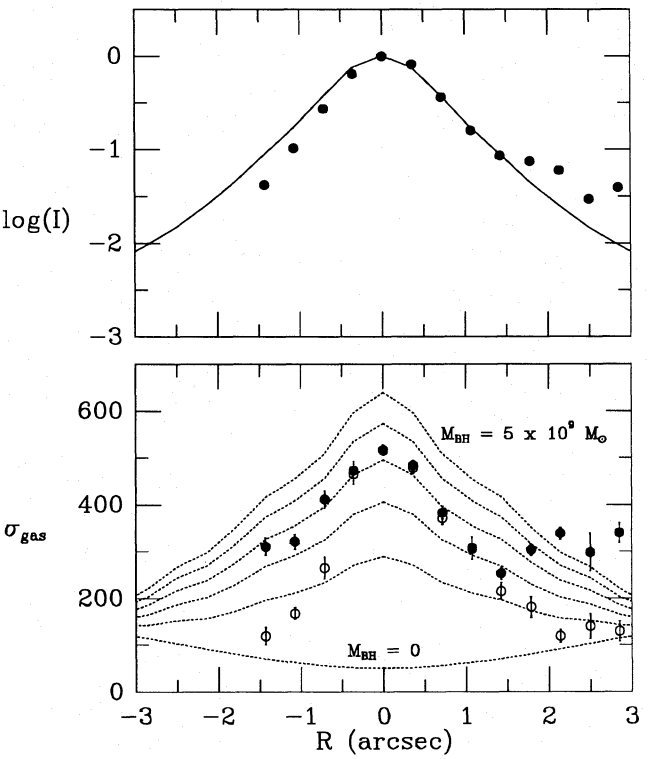

Figure 20. The top panel shows the Hγ flux along the slit, as in Fig. 19. The solid curve shows the (seeing-convolved and binned) predictions obtained by assuming the Hγ emissivity to be proportional to the gas mass density (equation 26). The curves in the bottom panel show the predicted (seeing-convolved and binned) velocity dispersions of spherical, isotropic, hydrostatic equilibrium models for the ionized gas, for black hole masses $M_{\rm BH} = 0$, 1, 2, 3, 4 and 5×10^9 M$_\odot$, respectively. The open data points show the velocity dispersion of the gas, as in Fig. 19. The solid data points show the rms motion $(V^2+\sigma^2)^{1/2}$.

predicted central velocity dispersion for the gas is very low (<100 km s^{-1}). The reason for this is that the gas is much more centrally concentrated than the potential in which it is embedded. To fit the observed central velocity dispersion, the presence of a central black hole is required. The three data points closest to the centre imply a black hole of mass $M_{\rm BH} = 3.3 \times 10^9$ M$_\odot$.

There might, of course, be many other (non-equilibrium) models for the gas kinematics that can explain the observed central velocity dispersion of the gas without requiring the presence of a black hole. None the less, it is interesting that the black hole mass inferred from our simple model is remarkably similar both to the black hole mass in our model C for the stellar kinematics and to the value $M_{\rm BH} = 2.6 \times 10^9$ M$_\odot$ deduced by Young et al. (1978) and Lauer et al. (1992) from models for the surface photometry. In the absence of more observational constraints on the geometry and density distribution of the gas, we decided not to study the gas kinematics in more detail.

11 CONCLUSIONS

We have obtained high S/N spectra of M87 in the spectral regions around the blue G-band and the IR Ca II triplet, in seeing of 0.79- and 0.63-arcsec FWHM, respectively. The spectra were analysed with a new method, based on χ^2-fitting the data in pixel space with the direct convolution of a template spectrum and a parametrized VP. This method was used to obtain estimates of the line strength, the mean and dispersion of the best-fitting Gaussian VP, and the Gauss–Hermite moments $h_3, \ldots h_6$.

The *HST* photometry of Lauer et al. (1992) was used to model the observed intensity profile along the slit. This allows an accurate determination of the contribution of the central luminosity spike to the observed light in each pixel. The nature of the central luminosity spike was then studied in two different ways. First, we estimated the spectrum of the spike directly, by modelling and subtracting the stellar light from the observed nuclear spectrum. Secondly, we modelled the observed line strengths, which we find to have a pronounced central minimum in both spectral regions. The results demonstrate that the central luminosity spike in M87 is completely non-thermal in both spectral regions. This disproves the claim of Jarvis & Melnick (1991) that the IR light of the spike is thermal.

We find that the kinematical quantities derived from the IR Ca II triplet data are less accurate than those derived from the blue G-band data. None the less, the main results derived from the two different spectral regions agree well. There is no sign of rotation along the position angle PA = 65° of our observations. Near the centre, there are indications of small deviations from the systemic velocity, but these are dynamically insignificant. The Gauss–Hermite moments $h_3, \ldots h_6$ are all consistent with zero, to within a few hundredths. The velocity dispersion rises from ~ 270 km s^{-1} at ~ 15 arcsec to ~ 305 km s^{-1} at ~ 5 arcsec, and then to ~ 400 km s^{-1} at 0.5 arcsec.

We determine the luminosity-density of M87 by deprojecting the *HST* photometry under the assumption of spherical symmetry. We then model the velocity dispersions derived from our blue data by solving the Jeans equation for radial hydrostatic equilibrium, adopting a suitably parametrized form for the velocity dispersion anisotropy function $\beta(r)$. Although our data are of higher spatial resolution than those used in previous studies, they can still be fitted equally well with radially anisotropic models without a central black hole as they can be with less anisotropic models with a central black hole. Our anisotropic models have $\beta(r) \leq 0.65$ everywhere, and hence do not require extreme anisotropies such as $\beta(r) = 0.9$ at $r = 2$ arcsec, as in the model of Binney & Mamon (1982).

In an attempt to construct anisotropic distribution functions for our Jeans equations solutions, we have considered a simple class of models for which the augmented mass density is a separable function of r and Ψ. We find, however, that the models for which the velocity dispersions fit the data have distribution functions that are not positive definite (i.e. they are unphysical). This might be due to the fact that we restrict ourselves to a special class of models, but it does illustrate that it is more difficult to fit the data with an actual distribution function than simply with an anisotropic solution of the Jeans equation.

An isotropic model with a 5×10^9 M$_\odot$ black hole fits the data in the central 5 arcsec reasonably well. Radial anisotropy, however, ($\beta_\infty \approx 0.5$) is required to fit the gradual decrease in the observed velocity dispersion for $R \gtrsim 5$ arcsec. We have made a study of the VPs of isotropic models for M87. In models with a central black hole, the central VP has wings that are more extended than those of a Gaussian. This is due to the stars that orbit close to the hole at high velocities, and hence most likely also true for anisotropic models with a central black hole. The wings contribute significantly to the normalization and the dispersion of the velocity profile. A Gaussian fit to the velocity profile is insensitive to the wings, and thus underestimates both the line strength γ and the velocity dispersion σ. In the analysis of real data, this effect is even more pronounced, because information on the wings is lost due to continuum subtraction. This might provide a natural explanation for two awkward features in our blue data, apparent also in the data of other authors: (i) the central line strength is too small to be accounted for solely by the dilution due to non-thermal light from the central luminosity spike, and (ii) the velocity dispersion in the centre is ~ 30 km s^{-1} smaller than that at $R \approx 0.5$ arcsec. Although our isotropic models do not describe these observations in detail, they do suggest the presence of a central black hole as a possible cause. In van der Marel (1994), it is shown that, for spectra to be obtained with *HST*, modelling of VP shapes will be even more important than for ground-based data.

We detected several emission lines in our M87 spectra and have made a detailed study of the kinematics of the Hγ line. The central velocity dispersion is very high at ~ 516 km s^{-1}, and drops steeply to ~ 125 km s^{-1} at $R = 2$ arcsec. Observations of previous authors, at much lower spatial resolution, showed a central velocity dispersion of only ~ 300 km s^{-1}. A simple hydrostatic equilibrium model for the ionized gas kinematics implies a black hole mass of $\sim 3 \times 10^9$ M$_\odot$. Although, admittedly, this model is naive, it is interesting that the inferred black hole mass is similar to that obtained from some of our models for the stellar kinematics, and to that obtained by other authors from models for the M87 surface photometry.

ACKNOWLEDGMENTS

The work presented here was carried out in the context of EARA, a European Association for Research in Astronomy, and is based on observations obtained with the William Herschel Telescope, which is operated on the island of La Palma by the Royal Greenwich Observatory in the Spanish Observatorio del Roque de los Muchachos of the Instituto de Astrofísica de Canarias. It is a pleasure to thank Dave Carter for assisting during the observations; Tim de Zeeuw, Marijn Franx, Hans-Walter Rix and Simon White for many stimulating discussions; Edward Qian for help with the discussion in Section 8; James Binney, Eric Emsellem and George Miley for commenting on an early version of this paper, and the institute for Advanced Study in Princeton for their hospitality during my stay in May 1993.

REFERENCES

Bacon R., Simien F., Monnet G., 1983, A&A, 128, 405
Bahcall J. N., Wolf R. A., 1976, ApJ, 209, 214
Binney J. J., Mamon G. A., 1982, MNRAS, 200, 361
Binney J. J., Tremaine S., 1987, Galactic Dynamics. Princeton Univ. Press, Princeton, NJ
Biretta J. A., Stern C. P., Harris D. E., 1991, AJ, 101, 1632
Boksenberg A. et al., 1992, A&A, 261, 393
Boroson T. A., Thompson I. B., 1991, AJ, 101, 111
Burbidge E. M., Burbidge G. R., Fish R. A., 1961, ApJ, 133, 393 (with erratum on p. 1092)
Carter D., Jenkins C. R., 1992, MNRAS, 257, 7P
Cohen J. G., 1978, ApJ, 221, 788
Crane P. et al., 1993, AJ, 106, 1371
Cuddeford P., 1991, MNRAS, 253, 414
Davies R. L., Birkinshaw M., 1988, ApJ, 68, 409
Davies R. L., Sadler E. M., Peletier R. F., 1993, MNRAS, 262, 650
Dehen W., 1993, MNRAS, 265, 250
Dejonghe H., 1987, MNRAS, 224, 13
Dejonghe H., 1989, in Merritt D., ed., Dynamics of Dense Stellar Systems. Cambridge Univ. Press, Cambridge, p. 69
de Vaucouleurs G., de Vaucouleurs A., Corwin H. G. Jr., Buta R. J., Paturel H. G., Fouqué P., 1991, 3rd Reference Catalogue of Bright Galaxies. Springer-Verlag, New York (RC3)
Dressler A., 1980, ApJ, 240, L11
Dressler A., Richstone D. O., 1990, ApJ, 348, 120
Duncan M. J., Wheeler J. C., 1980, ApJ, 237, L27
Efstathiou G., Ellis R. S., Carter D., 1980, MNRAS, 193, 931
Fabricant D., Gorenstein P., 1983, ApJ, 267, 535
Hardy E., Couture J., 1988, ApJ, 325, L29
Heckman T. M., Baum S. A., van Breugel W. J. M., McCarthy P., 1989, ApJ, 338, 48
Hénon M., 1973, A&A, 24, 229
Hunter C., Qian E., 1993, MNRAS, 262, 401
Jarvis B. J., 1990, A&A, 240, L8
Jarvis B. J., Melnick J., 1991, A&A, 244, L1
Jarvis B. J., Peletier R. F., 1991, A&A, 247, 315
Johnson H. L., 1965, ApJ, 141, 923
Kormendy J., 1992, ApJ, 388, L9
Kormendy J., 1993, in Beckman J. E., Netzer H., Colina L., eds, The Nearest Active Galaxies. Consejo Superior de Investigaciones Scientificas, Madrid
Kuijken K., Merrifield M. R., 1993, MNRAS, 264, 712
Larsen N., Nørgaard-Nielsen H. U., Kjærgaard P., Dickens R. J., 1983, A&A, 117, 257
Lauer T. R. et al., 1992, AJ, 103, 703
Léna P., 1988, Observational Astrophysics. Springer-Verlag, Berlin
Malkan M. A., Filippenko A. V., 1983, ApJ, 275, 477
Merritt D., 1985, AJ, 90, 1027
Merritt D., 1987, ApJ, 319, 55
Merritt D., Tremblay B., 1993, AJ, 106, 2229
Merritt D., Tremblay B., 1994, AJ, submitted
Mould J. R., Oke J. B., de Zeeuw P. T., Nemec J. M., 1990, AJ, 99, 1823
Newton A. J., Binney J. J., 1984, MNRAS, 210, 711
O'Connell R. W., 1973, AJ, 78, 1075
Oke J. B., Gunn J. E., 1983, ApJ, 266, 713
Osipkov L. P., 1979, Pis'ma Astr. Zh., 5, 77
Osterbrock D. E., Tran H. D., Veilleux S., 1992, ApJ, 389, 305
Palmer P., Papaloizou J., 1987, MNRAS, 224, 1043
Peletier R. F., 1989, PhD thesis, Univ. Groningen, Ch. 6
Peletier R. F., Davies R. L., Illingworth G. D., Davies L. E., Cawson M., 1990, AJ, 100, 1091
Pickles A. J., 1985a, ApJS, 59, 33
Pickles A. J., 1985b, ApJ, 296, 340
Press W. H., Flannery B. P., Teukolsky S. A., Vetterling W. T., 1989, Numerical Recipes. Cambridge Univ. Press, Cambridge
Pritchet C., 1977, ApJS, 35, 397
Qian E., 1993, PhD thesis, Florida State Univ.
Qian E., de Zeeuw P. T., van der Marel R. P., Hunter C., 1994, MNRAS, submitted
Richstone D. O., Sargent W. L. W., 1972, ApJ, 176, 91
Richstone D. O., Tremaine S., 1985, ApJ, 296, 370
Rix H. W., White S. D. M., 1992, MNRAS, 254, 389
Saha P., Williams T. B., 1994, AJ, 107, 1295
Sargent W. L. W., Young P. J., Boksenberg A., Shortridge K., Lynds C. R., Hartwick F. D. A., 1978, ApJ, 221, 731
Sharpless S., 1956, ApJ, 124, 342
Sparks W. B., Ford H. C., Kinney A. L., 1993, ApJ, 413, 531
Tremaine S., Richstone D. O., Byun Y. I., Dressler A., Faber, S. M., Grillmair C., Kormendy J., Lauer T. R., 1994, AJ, 107, 634
van der Marel R. P., 1994, ApJ, in press
van der Marel R. P., Franx M., 1993, ApJ, 407, 525 (vdMF)
van der Marel R. P., Rix H. W., Carter D., Franx M., White S. D. M., de Zeeuw P. T., 1994a, MNRAS, 268, 521 (Paper I)
van der Marel R. P., Evans N. W., Rix H. W., White S. D. M., de Zeeuw P. T., 1994b, MNRAS, in press (Paper II)
Winsall M. L., Freeman K. C., 1993, A&A, 268, 443
Young P. J., 1980, ApJ, 242, 1232
Young P., Westphal J. A., Kristian J., Wilson C. P., Landauer F. P., 1978, ApJ, 221, 721
Zeilinger W. W., Møller P., Stiavelli M., 1993, MNRAS, 261, 175

APPENDIX A: VELOCITY PROFILE FITTING IN PIXEL SPACE

Below, we discuss the algorithm used in Section 5 to determine line strengths, kinematics and VPs from observed galaxy spectra.

A1 The model for the galaxy spectrum

Let $G(x)$ and $S(x)$ be the logarithmically rebinned spectra of the galaxy and a star (or mix of stars), respectively. The quantity x is defined as $x \equiv \ln \lambda$. The Doppler shift resulting from a velocity dv is $dx = dv/c$, where c is the speed of light. The spectra are assumed to be sky-subtracted but not continuum-subtracted. The stellar spectrum is assumed to be normalized over the interval (x_1, x_M) for which data are available, i.e.

$$\frac{1}{x_M - x_1} \int_{x_1}^{x_M} S(x)\,dx = 1. \qquad \text{(A1)}$$

The following model is adopted for the galaxy spectrum:

$$G_{\rm mod}(x) \equiv a\left\{[B \circ S_\gamma](x) + \sum_{l=1}^{L} b_l \mathscr{P}_l(x)\right\}. \qquad \text{(A2)}$$

The free parameter a is a normalization factor. The first term inside the braces is the convolution of a broadening function $B(x)$ with a (normalized) template spectrum $S_\gamma(x)$, defined as

$$S_\gamma(x) \equiv \gamma S(x) + (1-\gamma). \qquad \text{(A3)}$$

The free parameter γ is called the 'line strength', and is invoked to allow for a possible difference in the equivalent width of the absorption lines between the galaxy spectrum $G(x)$ and the stellar spectrum $S(x)$. The second term inside the braces is a sum of continuum terms involving free parameters $b_1, \ldots b_L$. The $\mathscr{P}_l(x)$ are chosen to be the Legendre polynomials of order $1, \ldots L$ on the interval (x_1, x_M). They satisfy

$$\frac{1}{x_M - x_1} \int_{x_1}^{x_M} \mathscr{P}_n(x) \mathscr{P}_m(x)\, {\rm d}x = \delta_{mn}. \qquad \text{(A4)}$$

The lowest order Legendre polynomial $\mathscr{P}_0(x) \equiv 1$ is not included in the model because its contribution is embodied already in the parameter γ. The broadening function is $B(x) \equiv c\mathscr{L}(cx)$, where $\mathscr{L}(v)$ is the VP, i.e. the normalized distribution of stars over line-of-sight velocities. Following vdMF, we expand the VP in a Gauss–Hermite series with free parameters $(V, \sigma, h_3, \ldots h_N)$:

$$\mathscr{L}(v) = \frac{1}{\sigma}\alpha(w)\left[1 + \sum_{j=3}^{N} h_j H_j(w)\right],$$

$$w \equiv (v - V)/\sigma, \qquad \alpha(w) = \frac{1}{\sqrt{2\pi}} {\rm e}^{-(1/2)w^2}. \qquad \text{(A5)}$$

The functions H_l are the Hermite polynomials given in appendix A of vdMF.

We define functions $T_{j;V,\sigma}(x)$ as the convolutions

$$T_{j;V,\sigma}(x) \equiv \int_{-\infty}^{\infty} S(x')[c\alpha(w') H_j(w')/\sigma]\, {\rm d}x', \qquad \text{(A6)}$$

where we write $w' \equiv [c(x - x') - V]/\sigma$. Note that $T_{j;V,\sigma}(x) = T_{j;0,\sigma}(x - [V/c])$. Since $H_0(w) \equiv 1$, $T_{0;V,\sigma}(x)$ is simply the stellar spectrum $S(x)$ convolved with a Gaussian. We define constants k_j as

$$k_j \equiv \int_{-\infty}^{\infty} \alpha(y) H_j(y)\, {\rm d}y = \begin{cases} (j-1)!!/\sqrt{j!}, & (j \text{ even}), \\ 0, & (j \text{ odd}), \end{cases} \qquad \text{(A7)}$$

e.g. $k_0 = 1$, $k_4 = (1/4)\sqrt{6}$, $k_6 = (1/4)\sqrt{5}$. With these definitions, the model for the galaxy spectrum can be rewritten as

$$G_{\rm mod}(x) = a\left\{1 + \gamma(T_{0;V,\sigma}(x) - 1) + \sum_{j=3}^{N} h_j[k_j + \gamma(T_{j;V,\sigma}(x) - k_j)] + \sum_{l=1}^{L} b_l \mathscr{P}_l(x)\right\}. \qquad \text{(A8)}$$

In practice one has information on a discrete set of pixels $\{x_1, x_2, \ldots x_{M-1}, x_M\}$. The best fit to the galaxy spectrum is obtained when

$$\chi^2 \equiv \sum_{i=1}^{M} \left[\frac{G(x_i) - G_{\rm mod}(x_i)}{E(x_i)}\right]^2 \qquad \text{(A9)}$$

is minimized, where $E(x_i)$ is the (known) observational error in $G(x_i)$ that results from Poisson noise. Pixels containing emission lines or ill-subtracted sky lines are easily masked by removing them from the summation.

A2 Implementation

As in Paper I, we first determine the best-fitting Gaussian VP. Then we keep the parameters γ, V and σ of this fit fixed, and determine the best-fitting Gauss–Hermite series of order $N = 6$. This approach is justified by the fact that the Gauss–Hermite moments $h_3, \ldots h_6$ are essentially uncorrelated to γ, V and σ (vdMF).

To find the best-fitting Gaussian, we initially set $h_3 = \ldots = h_6 = 0$. We evaluate the functions $T_{0;0,\sigma}(x)$ for a representative set of velocity dispersions, e.g. σ running from 10 to 600 km s^{-1} with steps of a few km s^{-1}. This requires significant storage space, but not much computing time: to analyse all available galaxy data the convolutions have to be evaluated only once. The results can be used to obtain $T_{0;V,\sigma}(x)$ for any V, σ and x through interpolation. For any fixed combination of V and σ, the finding of the minimum $\chi^2_{\rm min}(V, \sigma)$ of χ^2 is a *linear* least-squares fitting problem for the parameters a, $a\gamma$, $ab_1, \ldots ab_L$. A routine was written that solves this problem by singular value decomposition (e.g. Press et al. 1989), hence allowing $\chi^2_{\rm min}(V, \sigma)$ to be calculated for any combination of V and σ. The problem then reduces to finding the V and σ that minimize $\chi^2_{\rm min}(V, \sigma)$. We solve this problem through a two-step iteration process. In the first step, the best-fitting V is found given a fixed guess for σ, and in the second step the best-fitting σ is found given a fixed guess for V. One starts with an initial guess for σ, and the first and second steps are then repeated alternately. This process converges within a few steps because the coefficients V and σ in a Gaussian fit are statistically uncorrelated (e.g. vdMF).

Having determined the best-fitting Gaussian, we keep γ, V and σ fixed and drop the constraint that $h_3 = \ldots = h_6 = 0$. We evaluate the functions $T_{j;V,\sigma}(x)$ for $j = 3, \ldots 6$. The minimization of χ^2 is then a linear least-squares fitting problem for the parameters a, $ah_3, \ldots ah_6$, $ab_1, \ldots ab_L$, which we also solve by singular value decomposition. The formal 1σ error bar on each parameter of the final fit is easily calculated as the change in that parameter required to increase χ^2 by one, with respect to its minimum value.

The functions $T_{j;V,\sigma}(x)$ are convolutions of the stellar spectrum $S(x)$ with functions of the form $c\alpha(w')H_j(w')/\sigma$. We evaluate these convolutions by taking the inverse Fourier transform of the product of the Fourier transforms of both functions. We always evaluate these (discrete) transforms on a much finer grid in x than the observed pixel grid, to make sure the functions $c\alpha(w')H_j(w')/\sigma$ are properly sampled.

We tested our software by reanalysing some of the data discussed in Paper I. The results agreed well with those obtained previously with the methods of Rix & White (1992) and vdMF.

A3 Template matching

In the method described above, it is important to use a spectrum $S(x)$ that best matches the spectral features of the galaxy spectrum $G(x)$. In practice one has an observed set of individual stellar spectra $\{S_k(x)\}_{k=1}^{K}$. We assume these spectra to be shifted to a common redshift. The most straightforward approach is to let $S(x)$ be a weighted sum of the $S_k(x)$,

$$S(x) = \sum_{k=1}^{K} c_k S_k(x). \qquad \text{(A10)}$$

Upon substitution in equations (A3) and (A2), this yields a model $G_{\rm mod}(x)$ that depends on an extra set of parameters, but only linearly. Although more storage space is required, this does not greatly increase the complexity of the χ^2 minimization problem. From a physical point of view, however, one wishes to constrain the c_k such that $c_k \in [0, 1]$ for all k. This makes the problem more complicated. We therefore opted for another approach, which uses the fact that the best-fitting template mix and the best-fitting kinematics are generally uncorrelated (Rix & White 1992).

For each stellar spectrum, we determine the best-fitting Gaussian VP. This yields, for each stellar spectrum $S_k(x)$, a best-fitting model $G_{{\rm mod},k}(x)$. An improved model for the galaxy spectrum is then constructed as

$$G_{\rm mod}(x) \equiv \sum_{k=1}^{K} c_k G_{{\rm mod},k}(x), \qquad \text{(A11)}$$

where the $c_k \in [0, 1]$ are free parameters. The 'biased random walk' minimization algorithm described in the appendix of Rix & White (1992) is used to determine the c_k that minimize the χ^2 in equation (A9), with $G_{\rm mod}(x)$ as in equation (A11). The best matching spectrum $S(x)$ is then taken to be as in equation (A10). This spectrum is used to determine the final fit to the galaxy spectrum.

Table B1. M87, PA = 65°, Hγ ionized gas kinematics.

r	I	ΔI	V	ΔV	σ	$\Delta\sigma$
-1.43	0.042	0.006	-287.0	18.6	119.4	18.7
-1.07	0.102	0.007	-273.8	17.8	167.2	12.5
-0.71	0.273	0.011	-315.0	20.1	264.7	23.5
-0.36	0.637	0.015	-78.6	14.9	465.4	21.2
0.00	1.000	0.017	10.6	11.4	516.2	11.5
0.36	0.815	0.015	74.1	12.1	478.1	11.2
0.71	0.362	0.011	98.0	13.2	370.5	13.1
1.07	0.161	0.009	-20.5	24.0	306.0	23.8
1.43	0.086	0.007	-134.6	25.5	214.6	17.6
1.78	0.075	0.007	-243.4	24.9	180.3	22.3
2.14	0.060	0.005	-316.3	15.0	118.9	13.8
2.50	0.030	0.006	-263.2	40.4	139.7	26.3
2.86	0.039	0.006	-313.8	21.2	129.0	21.1

APPENDIX B: IONIZED GAS (Hγ) KINEMATICS

Table B1 lists the total intensity, mean velocity and velocity dispersion of the Hγ emission line, as displayed in Fig. 19. The radius r is the galactocentric distance along the slit. Positive radii lie in the direction of the indicated position angle. The quantities V and σ are in km s^{-1}. The intensity was scaled to unity in the centre.

APPENDIX C: STELLAR KINEMATICS

Tables C1 and C2 list the results displayed in Figs 4(a) and (b). The radius $\bar{r}$ is the galactocentric distance along the slit. In the outer parts, where several galaxy spectra were binned together, $\bar{r}$ is the intensity-weighted average radius of the binned spectra.

Table C1. M87, PA = 65°, blue G-band stellar kinematics and velocity profile shapes.

$\bar{r}$	γ	$\Delta\gamma$	V	ΔV	σ	$\Delta\sigma$	h_3	Δh_3	h_4	Δh_4	h_5	Δh_5	h_6	Δh_6
-23.27	0.877	0.023	3.1	7.1	260.2	10.7	-0.002	0.029	-0.014	0.028	-0.054	0.032	-0.029	0.031
-17.02	0.871	0.023	-11.1	7.8	256.9	10.3	-0.003	0.029	-0.057	0.028	-0.045	0.032	0.031	0.031
-13.88	0.882	0.022	-16.4	6.8	251.8	11.1	-0.035	0.028	0.067	0.028	-0.038	0.032	-0.043	0.031
-11.76	0.963	0.023	8.3	15.1	297.8	11.6	-0.078	0.026	0.000	0.024	-0.026	0.027	0.000	0.027
-10.16	0.907	0.023	13.2	9.6	302.1	12.1	0.015	0.027	0.012	0.024	-0.043	0.027	-0.009	0.028
-8.91	0.926	0.022	-18.9	8.5	278.0	10.7	-0.036	0.026	-0.003	0.025	0.047	0.028	-0.008	0.028
-7.84	0.979	0.021	-7.9	8.2	291.1	8.9	-0.021	0.022	-0.059	0.021	0.007	0.023	0.039	0.024
-6.96	0.910	0.023	21.0	7.1	285.9	10.7	-0.053	0.027	-0.084	0.025	0.003	0.029	0.078	0.029
-6.24	0.981	0.023	1.2	11.0	320.5	10.9	0.002	0.024	-0.028	0.021	-0.069	0.023	-0.033	0.023
-5.53	0.963	0.021	-3.4	8.5	310.6	10.8	-0.012	0.023	0.024	0.021	-0.006	0.023	-0.053	0.023
-4.82	0.898	0.019	15.2	8.4	298.4	9.9	0.033	0.023	-0.028	0.021	-0.015	0.024	0.041	0.024
-4.10	0.980	0.019	-1.5	9.1	324.2	10.1	0.014	0.021	0.026	0.018	-0.015	0.020	-0.001	0.020
-3.39	0.966	0.018	8.6	7.9	323.2	9.0	-0.017	0.019	-0.004	0.017	-0.030	0.019	-0.029	0.019
-2.86	0.919	0.024	-0.3	8.2	324.7	12.3	-0.042	0.027	-0.035	0.024	-0.014	0.026	-0.003	0.026
-2.50	0.928	0.023	-2.2	9.3	321.4	11.7	-0.014	0.026	-0.046	0.023	-0.002	0.026	0.046	0.026
-2.14	0.985	0.023	-7.9	8.9	351.4	11.8	-0.017	0.024	-0.053	0.022	-0.018	0.023	0.020	0.022
-1.78	0.983	0.023	1.6	8.4	364.5	13.7	-0.017	0.024	0.040	0.022	-0.002	0.023	-0.021	0.022
-1.43	0.947	0.022	-20.7	8.5	361.0	12.8	-0.013	0.024	0.009	0.021	-0.023	0.023	-0.032	0.022
-1.07	0.943	0.021	-21.6	7.3	369.5	12.8	-0.010	0.023	0.023	0.021	0.010	0.022	-0.011	0.020
-0.71	0.813	0.019	-8.6	10.7	396.7	13.8	-0.040	0.023	0.003	0.021	0.032	0.022	-0.014	0.021
-0.36	0.603	0.015	-33.9	12.9	403.1	14.2	-0.063	0.024	-0.027	0.023	0.037	0.024	0.026	0.022
0.00	0.463	0.012	-22.9	9.3	374.9	14.8	-0.040	0.026	0.010	0.024	0.010	0.025	-0.050	0.024
0.36	0.543	0.014	-2.5	8.4	361.5	14.0	0.020	0.026	0.026	0.023	-0.004	0.024	-0.063	0.023

Table C1 – *continued*

$\bar{r}$	γ	$\Delta\gamma$	V	ΔV	σ	$\Delta\sigma$	h_3	Δh_3	h_4	Δh_4	h_5	Δh_5	h_6	Δh_6
0.71	0.807	0.019	31.5	9.1	399.6	14.0	-0.032	0.023	0.009	0.022	0.045	0.023	-0.003	0.021
1.07	0.932	0.020	-6.6	8.2	359.5	12.0	-0.026	0.022	0.007	0.020	-0.001	0.021	-0.034	0.020
1.43	0.971	0.022	-4.2	12.3	371.6	12.1	-0.038	0.023	-0.041	0.021	-0.034	0.022	-0.006	0.021
1.78	0.967	0.024	1.9	9.3	371.9	13.6	-0.029	0.025	-0.016	0.023	0.032	0.024	0.038	0.023
2.14	0.962	0.023	-1.2	12.3	341.2	12.1	-0.012	0.025	-0.026	0.022	0.018	0.024	0.000	0.023
2.50	0.972	0.024	-1.2	12.3	339.0	12.9	-0.042	0.026	-0.005	0.023	-0.009	0.025	-0.014	0.024
2.86	0.928	0.025	-28.8	11.8	334.7	13.1	-0.007	0.027	-0.022	0.024	-0.034	0.026	-0.002	0.026
3.39	0.969	0.018	16.1	6.8	320.9	8.9	-0.022	0.019	-0.017	0.017	0.011	0.019	0.011	0.019
4.10	0.986	0.019	-14.6	9.8	325.4	9.5	-0.053	0.020	-0.033	0.018	-0.031	0.019	0.006	0.019
4.82	0.921	0.019	-8.5	8.9	298.6	10.1	-0.060	0.022	0.030	0.020	0.065	0.022	-0.039	0.023
5.53	0.973	0.021	9.3	7.7	319.6	11.3	-0.067	0.023	0.028	0.021	0.031	0.023	-0.032	0.023
6.24	0.923	0.022	2.7	10.7	301.8	10.7	0.016	0.025	-0.049	0.023	-0.034	0.026	0.043	0.026
6.96	0.937	0.024	0.0	12.3	311.6	11.8	0.040	0.027	-0.030	0.024	0.002	0.027	0.016	0.027
7.84	0.948	0.021	0.2	8.4	299.7	10.0	0.039	0.023	-0.024	0.021	-0.059	0.024	0.015	0.024
8.92	0.949	0.022	-4.6	9.1	280.3	10.3	0.025	0.026	-0.024	0.024	0.010	0.028	0.040	0.028
10.16	0.952	0.022	3.1	8.9	276.6	9.6	-0.035	0.024	-0.028	0.023	-0.030	0.026	-0.019	0.026
11.76	0.908	0.023	22.1	10.1	286.2	11.6	-0.045	0.027	0.002	0.025	-0.076	0.028	-0.028	0.028
13.88	0.930	0.024	-6.8	10.7	294.2	12.3	-0.013	0.027	0.051	0.025	0.015	0.028	-0.060	0.029
17.03	0.904	0.024	2.9	7.8	280.1	11.2	0.039	0.028	-0.047	0.027	-0.029	0.030	0.063	0.031
23.31	0.855	0.022	-5.8	8.7	244.9	10.7	-0.037	0.030	0.046	0.029	0.002	0.034	-0.032	0.031

Table C2. M87, PA= 65°, IR Ca II triplet stellar kinematics and velocity profile shapes.

$\bar{r}$	γ	$\Delta\gamma$	V	ΔV	σ	$\Delta\sigma$	h_3	Δh_3	h_4	Δh_4	h_5	Δh_5	h_6	Δh_6
-22.51	0.627	0.029	3.1	19.1	219.0	15.9	-0.046	0.048	0.007	0.043	0.044	0.050	0.017	0.045
-17.84	0.620	0.029	12.9	10.1	228.4	17.4	0.059	0.049	0.028	0.045	-0.101	0.052	-0.007	0.045
-15.03	0.601	0.031	10.5	9.5	250.1	17.6	-0.008	0.049	-0.026	0.046	0.009	0.054	-0.015	0.046
-13.04	0.595	0.031	-11.6	12.9	247.4	19.4	0.049	0.051	0.028	0.047	-0.062	0.057	-0.048	0.047
-11.54	0.562	0.032	29.0	21.4	261.6	19.9	-0.002	0.053	-0.046	0.051	-0.027	0.060	0.003	0.053
-10.20	0.528	0.027	-24.8	12.9	242.0	19.9	-0.084	0.052	0.053	0.048	-0.034	0.058	-0.034	0.048
-9.04	0.617	0.031	1.6	10.7	272.9	20.0	-0.118	0.048	0.005	0.046	-0.003	0.055	0.005	0.049
-8.03	0.616	0.031	-0.9	12.3	290.7	21.0	-0.058	0.044	0.040	0.042	0.077	0.050	-0.069	0.047
-7.20	0.626	0.035	-10.1	10.7	292.3	22.1	-0.063	0.050	-0.003	0.047	-0.042	0.056	-0.018	0.054
-6.53	0.655	0.034	-9.4	16.1	304.0	22.8	0.019	0.047	0.024	0.043	-0.084	0.051	-0.005	0.051
-5.86	0.615	0.034	32.1	11.8	313.6	23.2	-0.048	0.047	-0.016	0.042	0.024	0.050	0.024	0.052
-5.19	0.613	0.032	-17.8	16.1	312.4	21.1	-0.069	0.045	-0.018	0.040	0.021	0.048	-0.001	0.048
-4.52	0.747	0.032	-18.0	19.1	337.5	19.5	-0.044	0.037	0.000	0.032	-0.036	0.037	0.008	0.037
-3.85	0.626	0.029	1.6	17.4	309.5	18.9	-0.053	0.040	-0.030	0.036	0.026	0.043	0.025	0.043
-3.18	0.653	0.030	-8.0	11.0	341.5	20.5	-0.038	0.038	0.001	0.033	-0.015	0.038	-0.015	0.038
-2.68	0.747	0.046	-14.3	42.7	386.5	26.4	0.016	0.047	-0.086	0.043	-0.031	0.048	0.069	0.043
-2.35	0.743	0.046	11.5	11.8	395.3	29.9	0.032	0.047	-0.028	0.044	-0.014	0.049	0.041	0.043
-2.01	0.589	0.038	9.6	19.1	328.9	27.0	0.025	0.054	-0.037	0.047	-0.034	0.055	0.043	0.057
-1.67	0.639	0.039	19.4	10.7	356.3	29.1	0.013	0.049	-0.003	0.043	0.029	0.050	-0.002	0.049
-1.34	0.572	0.037	-8.8	11.4	345.7	28.1	-0.049	0.052	-0.017	0.045	-0.022	0.052	-0.023	0.052
-1.00	0.560	0.035	-5.5	12.3	343.5	24.2	-0.017	0.049	-0.069	0.042	-0.014	0.049	-0.019	0.049
-0.67	0.527	0.036	19.0	17.4	387.3	32.0	-0.097	0.053	-0.041	0.049	0.096	0.056	0.081	0.050
-0.34	0.448	0.030	-3.1	12.9	368.7	31.7	-0.009	0.053	-0.009	0.047	0.061	0.053	0.018	0.050
0.00	0.417	0.030	-61.6	17.4	413.0	36.2	0.007	0.054	-0.009	0.052	-0.044	0.058	0.018	0.050
0.34	0.491	0.034	-26.0	16.1	428.4	39.8	-0.056	0.051	0.048	0.051	-0.024	0.058	0.003	0.049
0.67	0.561	0.038	-20.5	16.1	410.2	33.6	-0.035	0.049	0.004	0.047	-0.020	0.054	-0.013	0.046
1.00	0.563	0.036	8.9	30.2	357.5	26.6	0.016	0.052	-0.084	0.045	-0.024	0.052	0.091	0.051
1.34	0.585	0.037	-15.3	16.1	352.7	29.2	-0.127	0.053	0.004	0.046	-0.015	0.053	0.013	0.052
1.67	0.701	0.043	37.8	10.7	392.0	32.1	-0.026	0.046	0.033	0.043	0.011	0.049	-0.036	0.043
2.01	0.636	0.042	48.1	21.4	367.5	29.2	-0.022	0.052	-0.052	0.046	0.005	0.053	0.070	0.051
2.35	0.685	0.044	-12.9	12.3	376.1	32.0	-0.085	0.052	0.011	0.047	-0.017	0.053	0.060	0.049
2.68	0.574	0.039	5.4	16.1	322.5	26.3	-0.009	0.057	-0.055	0.050	-0.058	0.059	0.014	0.060
3.18	0.613	0.028	10.8	11.8	313.0	17.0	0.012	0.038	-0.073	0.034	-0.037	0.041	0.024	0.042
3.85	0.670	0.030	4.4	16.1	327.9	18.9	0.010	0.038	-0.030	0.033	-0.020	0.039	-0.007	0.040
4.52	0.674	0.031	5.6	9.5	326.9	22.1	-0.037	0.040	0.041	0.035	-0.057	0.041	-0.040	0.042
5.19	0.749	0.035	-12.2	12.9	354.2	21.7	-0.083	0.038	0.000	0.034	0.050	0.038	0.000	0.037
5.86	0.670	0.034	-9.9	12.3	317.9	20.5	0.012	0.043	-0.048	0.038	0.024	0.045	0.016	0.046
6.53	0.685	0.037	-14.9	13.5	329.0	24.9	-0.008	0.046	0.016	0.040	0.026	0.047	-0.016	0.048

Table C2 – *continued*

$\bar{r}$	γ	$\Delta\gamma$	V	ΔV	σ	$\Delta\sigma$	h_3	Δh_3	h_4	Δh_4	h_5	Δh_5	h_6	Δh_6
7.20	0.625	0.032	-15.7	11.8	265.1	21.8	-0.057	0.050	0.042	0.048	0.013	0.058	-0.027	0.049
8.03	0.606	0.028	-0.1	11.4	263.4	18.4	0.021	0.045	-0.006	0.043	0.040	0.052	0.044	0.044
9.04	0.691	0.034	12.6	16.1	299.3	18.4	-0.003	0.042	-0.066	0.039	0.016	0.047	0.025	0.047
10.20	0.602	0.028	-5.6	12.9	255.6	17.9	-0.011	0.046	-0.024	0.044	-0.063	0.053	0.044	0.044
11.54	0.592	0.032	5.1	15.1	251.3	23.5	-0.004	0.053	0.121	0.050	-0.147	0.060	-0.085	0.050
13.04	0.738	0.033	-5.3	10.7	264.8	15.2	0.056	0.042	-0.075	0.040	-0.068	0.048	0.053	0.041
15.03	0.560	0.030	15.7	10.7	232.2	20.1	-0.075	0.054	0.080	0.049	-0.002	0.057	-0.084	0.049
17.84	0.583	0.032	3.8	10.7	245.5	19.9	-0.076	0.052	0.042	0.049	-0.006	0.058	-0.085	0.048
22.52	0.613	0.033	14.1	21.4	260.7	19.5	-0.001	0.050	-0.004	0.048	-0.037	0.057	-0.035	0.049